

Simulation of tsunami induced by a submarine landslide in a glaciomarine margin: the case of Storfjorden LS-1 (Southwestern of the Svalbard Islands)

María Teresa Pedrosa-González¹, José Manuel González-Vida ², Jesús Galindo-Záldivar ^{1,4}, Sergio
5 Ortega², Manuel Jesús Castro³, David Casas⁵, Gemma Ercilla⁵.

¹Departamento de Geodinámica, Universidad de Granada, 18071 Granada, Spain.

²Departamento de Matemática Aplicada, Escuela de Ingenierías Industriales, Universidad de Málaga, 29071 Málaga, Spain.

³Departamento de Análisis Matemática, Estadística e I.O y Matemática Aplicada, Facultad de Ciencias, Universidad de Málaga, 29071 Málaga, Spain.

10 ⁴Instituto Andaluz de Ciencias de La Tierra (CSIC-UGR), Granada, Spain Instituto Andaluz de Ciencias de la Tierra (CSIC-UGR).

⁵Institut de Ciències del Mar, CSIC., 08003 Barcelona, Spain.

Correspondence to: Gemma Ercilla (gemma@icm.csic.es)

15 **Abstract.**

A modelling approach to understand the tsunamigenic potentiality of submarine landslides will provide new perspectives on tsunami hazard threat, mostly in polar margins where global climatic change and its related ocean warming may induce future landslides. Here, we use the Landslide L-ML-HySEA numerical model, including wave dispersion, to provide new insights in factors controlling the tsunami characteristics triggered by the Storfjorden LS-1 landslide (Southwestern Svalbard). Tsunami
20 waves, determined mainly by the sliding mechanism and the bathymetry, consist of two initial wave dipoles, with troughs to the northeast (Spitsbergen and towards the continent) and crests to the south (seawards) and southwest (Bear Island), reaching more than 3 m of amplitude above the landslide, and finally merging into a single wave dipole. The tsunami wave propagation and its coastal impact are governed by the Storfjorden and Kveithola glacial troughs, and by the bordering Spitsbergen Bank, which shape the continental shelf. This local bathymetry controls the direction of propagation with a crescent shape front, in
25 plan view, and is responsible for shoaling effects amplitude values (4.2 m in trough to 4.3 m in crest), amplification (3.7 m in trough to 4 m in crest), diffraction of the tsunami waves, as well as influencing their coastal impact times.

1 Introduction

Submarine landslides represent one of the most common potential offshore geohazards in the continental slopes of the northern
30 high-latitude margins (Elverhøi et al., 2002; Lee et al., 2009). There, the slope failures are essentially focused at their trough mouth fans (Dowdeswell et al., 2008; Rebesco et al., 2014; Llopart et al., 2016; Ercilla et al., 2022, and references therein). Some landslides may also cause tsunamis, as it has been evidenced for the Storegga landslide (3000 km³, at 8.1 kyr), with wave amplitudes of ~20 m at the shore (Bondevik et al. 2003; Haflidason et al., 2005; Kvalstad et al. 2005), or the Hinlopen

landslide (1150 km³, at 30 kyr) with wave amplitudes of ~40 m (a.s.l.) (Winkelmann et al., 2008; Vanneste et al., 2006).
35 In the Fram Strait (500 to 1000 km³), located between the main ice retreat areas of Greenland and Svalbard, that triggered
waves of up to 5.6 m (Berndt et al., 2009). The factors controlling slope failures in the northern high-latitude margins are still
not fully understood. The most common causal factors are the interlayering of underconsolidated glacially derived sediments
and low permeability interglacial hemipelagic clay rich layers, combined with tectonic and isostatic related seismicity and/or
gas hydrate dissociation (Kvalstad et al., 2005; Canals et al., 2004; Sierro et al., 2009; Garcia et al., 2011; Casas et al., 2013;
40 Vanneste., 2014; Moernaut et al., 2017; Llopart et al., 2019).

The understanding of the tsunamigenic potential of submarine landslides still needs to be improved (Chiocci and
Ridente, 2011; Løvholt et al., 2020). In this sense back analysis of specific events is commonly used to advance their
understanding, as well as to contribute to the hazard assessments of future landslides (Macias et al., 2015; Rodriguez et al.,
2019; Sun and Leslie, 2020; Innocenti et al., 2021). In the European northern high-latitude margins, e.g. Svalbard and
45 Greenland coasts, the tsunami threat has been assessed for a few past landslides. It is important to point out that the tsunami
geohazard associated with Holocene landslides such as the Bjørnøyrenna (Laberg and Vorren, 1993), which is the largest
landslide (volume of about 1100 km³) in the Barents Sea continental margin, the Nyk landslide in central Norway (Lindberg
et al., 2004), or the giant Andøya landslide (north-eastern Norwegian–Greenland Sea) (Bugge et al., 1987; Laberg et al 2000),
have not been accurately modelled. The tsunami modelling of recent landslides in this region is important, because it will allow
50 us to infer the tsunami potential of future landslides due to climate change and its related ocean warming. Both those
interconnected issues are significantly affecting the northern high latitude margins, and may contribute to an increase in the
occurrence of submarine landslides, both large and small, in the nearby future, mostly due to gas hydrate dissociation and
isostatic rebound related earthquakes (Maslin et al., 1998; Tappin, 2010; Urlaub et al., 2014).

Today, the archipelago of Svalbard is one the fastest warming areas of the Arctic Ocean, experiencing an increase in
55 the melting of their glaciers and a rise in the temperature of ocean water circulating along its continental margin (Meleshko, et
al., 2004; Førland et al., 2013; Skogseth, 2020). This fact may provide adequate conditions to trigger unloading earthquakes,
and to increase pore water pressure by gas hydrate breakdown, which can destabilize slope sediments (Solheim et al., 2005;
Berndt et al., 2009), i.e., the occurrence of landslides and tsunamis in the near future. Both landslides and tsunamis may
represent a danger to offshore infrastructures, associated with present and future hydrocarbons exploitation and other
60 renewable energies (Zhang et al., 2019). Tsunamis may also have an impact on the coastal areas of the nearby regions of NW
Europe, considering the increasing human pressures of these areas (Imamura et al., 2019). The geological record of the
Svalbard continental margin can help us to assess the possible tsunamis induced by future landslides. In fact, the sedimentary
record of its continental slope evidences numerous landslides, such as the Storfjorden LS-1 landslide, which forms part of the
Storfjorden trough mouth fan, and even other recent landslides located in the interfan area of the Storfjorden and Kveithola
65 trough mouth fans (TMFs) (Pedrosa et al., 2011; Rebesco et al., 2012; Lucchi et al., 2012; Llopart et al 2015).

The tsunami potential of relative medium size as Storfjorden LS-1 provides new insights in tsunami wave characteristics
and evolution. It will help to better understand possible future tsunami hazard in high latitudes. Geomorphic and geotechnical

data have been integrated in the L-ML-HySea landslide tsunamigenic model simulating landslide dynamics, tsunami wave generation, propagation and coastal impact.

70

2 Geological Setting

The Svalbard is located west of the epi-continental Barents Sea and Norwegian continental margin (Fig. 1a). The archipelago resulted from the opening of the northern Atlantic. The major NW-SE fault zone are associated with the Knipovich Ridge, the Hornsund Fault Zone (HFZ) crossing the Spitsbergen Island and spreads western of the Barents (Worsley, 1986; Eiken et al., 1994; Engen et al., 2008; Faleide et al., 2008) (Fig. 1b). The post-rift activity of these fault zones has contributed to deform the Plio-Pleistocene sedimentary sequence (Faleide et al., 1993, 2008; Fiedler and Faleide, 1996). This fault zone have been reactivated by isostatic loading and unloading rebound periods (Pirli et al., 2013; Newton and Huuse, 2017) that are responsible for the local seismicity in the continental margin, and can become the trigger of slope failures (Hampel et al., 2009; L'Heureux et al., 2013; Bellwald et al., 2016). Historical earthquakes with magnitudes up to $M_w \sim 5$ have been recorded (Auriac et al., 2016) (Fig. 1c).

The northwestern Barents continental slope is affected by the Storfjorden and Kveithola (TMFs), (Fig. 2), created by the high sediment input from the Storfjorden and Kveithola glacial troughs crossing the continental shelf, during the onset of the major Northern Hemisphere Glaciations, around 2.6-2.7 Ma (Faleide et al., 1996; Butt et al., 2000; Knies et al., 2009). The Storfjorden TMF seafloor is shaped by the relatively large Storfjorden landslide (SL1) that extends from the shelf-edge to the lower continental slope. In spite of their fresh morphological expression, the seismic stratigraphy indicates that SL1 (Fig. 3c) is a palaeolandslide above the 0.2 Ma R1 reflector (Rebesco et al., 2012), that is then draped by a regional 100 ms (~ 8 m, considering 1600 m/s sediment velocity) thick sediment units (Lucchi et al., 2012; Llopart et al., 2015), and the sliding mass is a subtabular depositional body, between 3 and 5 ms thick (Pedrosa et al., 2011). The high-resolution seismic stratigraphy in the southern Storfjorden TMF is dominated mainly by an alternation of acoustically stratified and transparent units. Eight seismic stratigraphy units (A to G, from top to bottom) have been identified above the reflector R1 (Fig. 3c). Based on acoustic facies they are as follow: the stratified units A, C, E and G and the transparent units B, D and F. The stratified units are usually continuous with high amplitude and draping the existing topography, while the transparent units present an irregular upper boundary and usually a basal erosive surface that describe individual lenses. Comparable seismic facies have also been found in others TMFs (Laberg and Vorren et al., 1995; Ó Cofaigh et al., 2003).

100

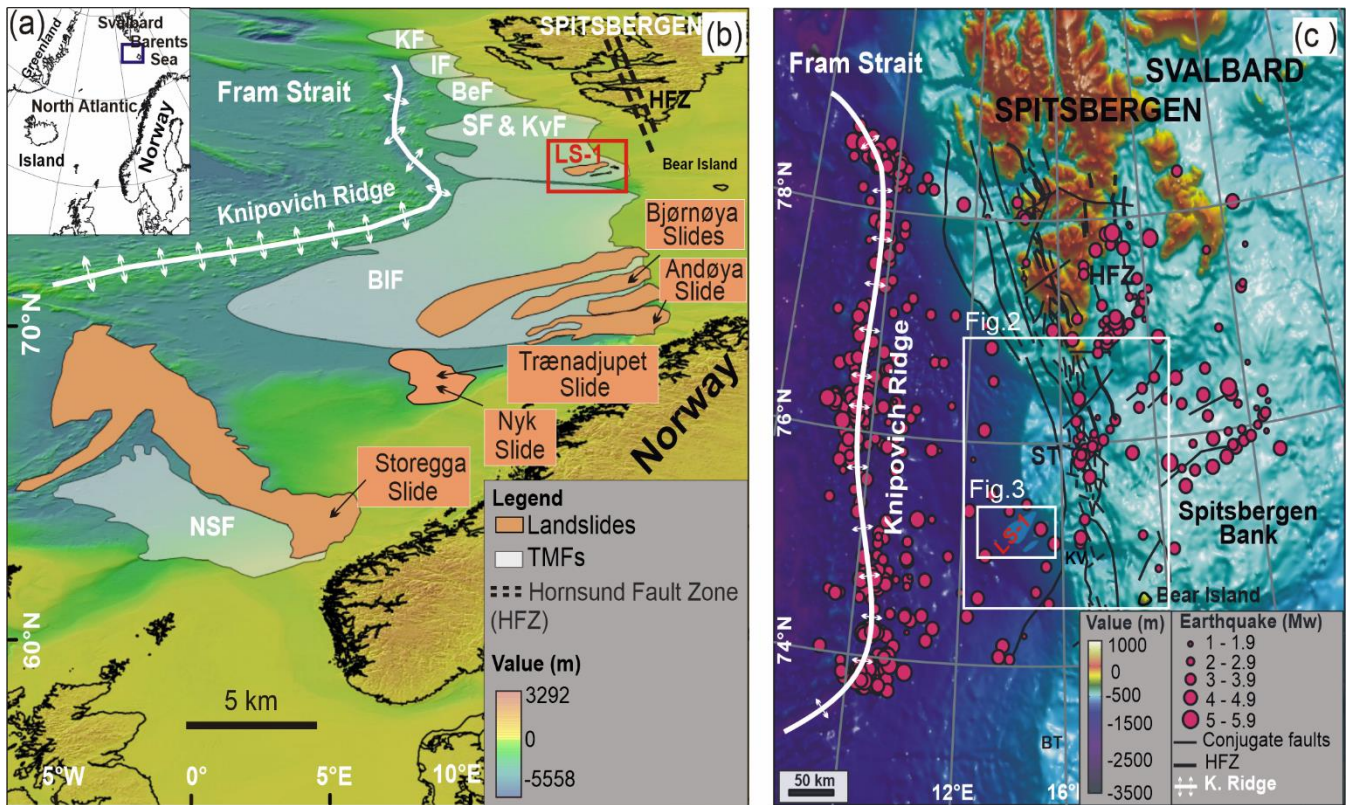


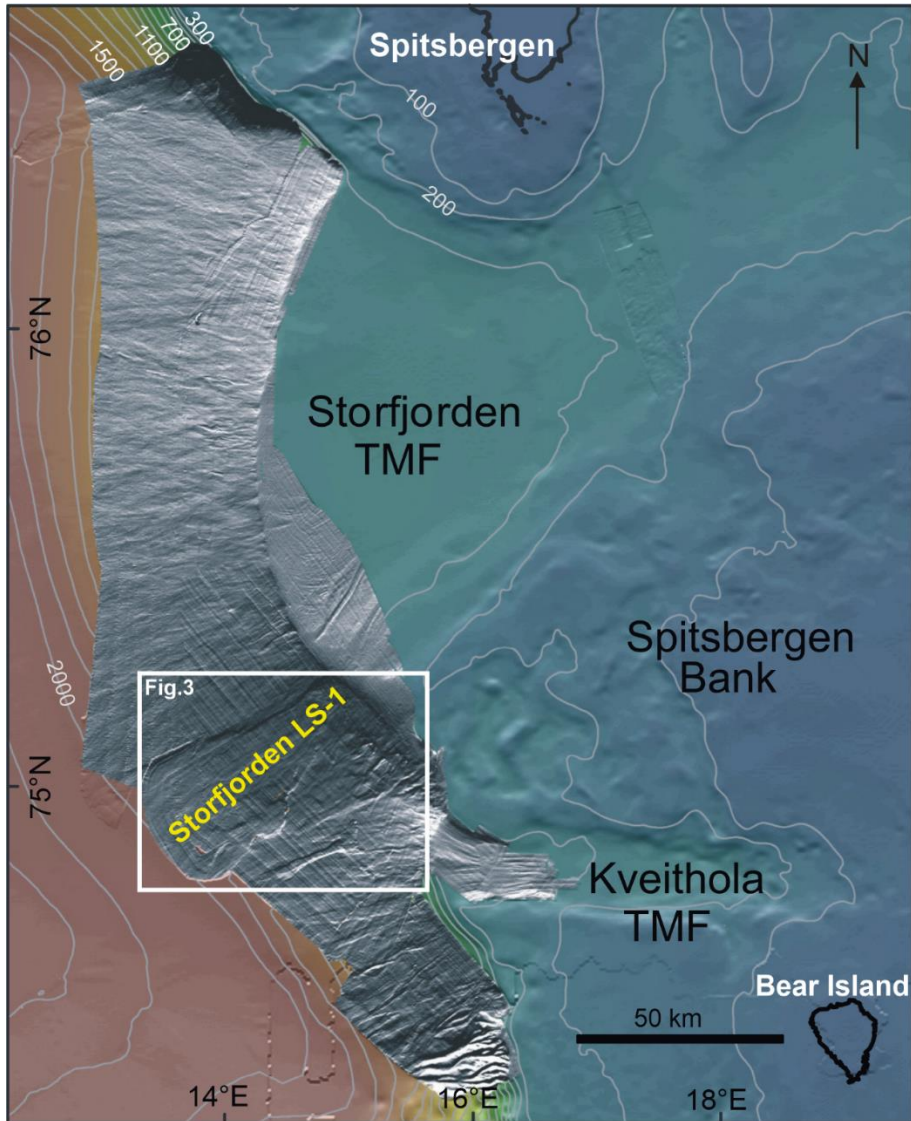
Figure 1. Geographic and geological settings of Storfjorden LS-1. (a) Location map of the study area (blue rectangle). (b) Shaded relief map taken from the International Bathymetric Chart of the Arctic Ocean (IBCAO) version 3.0 (Jakobsson et al., 2012) of North Atlantic Ocean (Norwegian and Barents Sea). The major Trough Mouth Fans (grey polygons), and the major submarine landslides (orange polygons) are located in the map. Compilation from : Haflidason et al. (2005); Laberg et al. (2000); Laberg and Vorren, (2000, 1993); Lindberg et al. (2004); Sejrup et al. (2005), and references therein. KF: Kongsfjorden Fan; IF: Isfjorden Fan; BeF: Bellsund Fan; SF & KvF Storfjorden and Kveithola Fans; BIF: Bear Island Fan; NSF: North Sea Fan. (c) Shaded relief map of northwestern Barents Sea (Ottesen et al., 2016) displaying the location of the Hornsund Fault Zone (HFZ) and the historical earthquakes recorded from 1960 to 2018 (source from IRIS catalogue). This map also shows the locations of figures 2 and 3.

3 Dataset and Methods

3.1. Bathymetric data

For slide modelling, high-resolution multibeam bathymetry data-sets from different cruises (SVAIS onboard BIO Hespérides, 2007; and EGLACOM onboard R/V Explora 2008) have been integrated (Fig. 2). Data processing consisted of cleaning and

120 filtering the navigation data, noise reduction, and data editing using Caris HIPS and SIPS software. Data were gridded at 75 m and partially cover the Storfjorden and Kveithola TMFs (~15,300 km²). The bathymetric mosaic was completed with lower resolution bathymetry data at 250 m provided by Norwegian Hydrography Survey (NHS); these were collected between 1965 and 1985 (Ottessen et al., 2006). Moreover, regional gridded bathymetry data for the Arctic Ocean area (IBCAO; <https://gebco.net>) interpolated to 2.5 km bin size, were only used for regional figures (Fig. 1b).



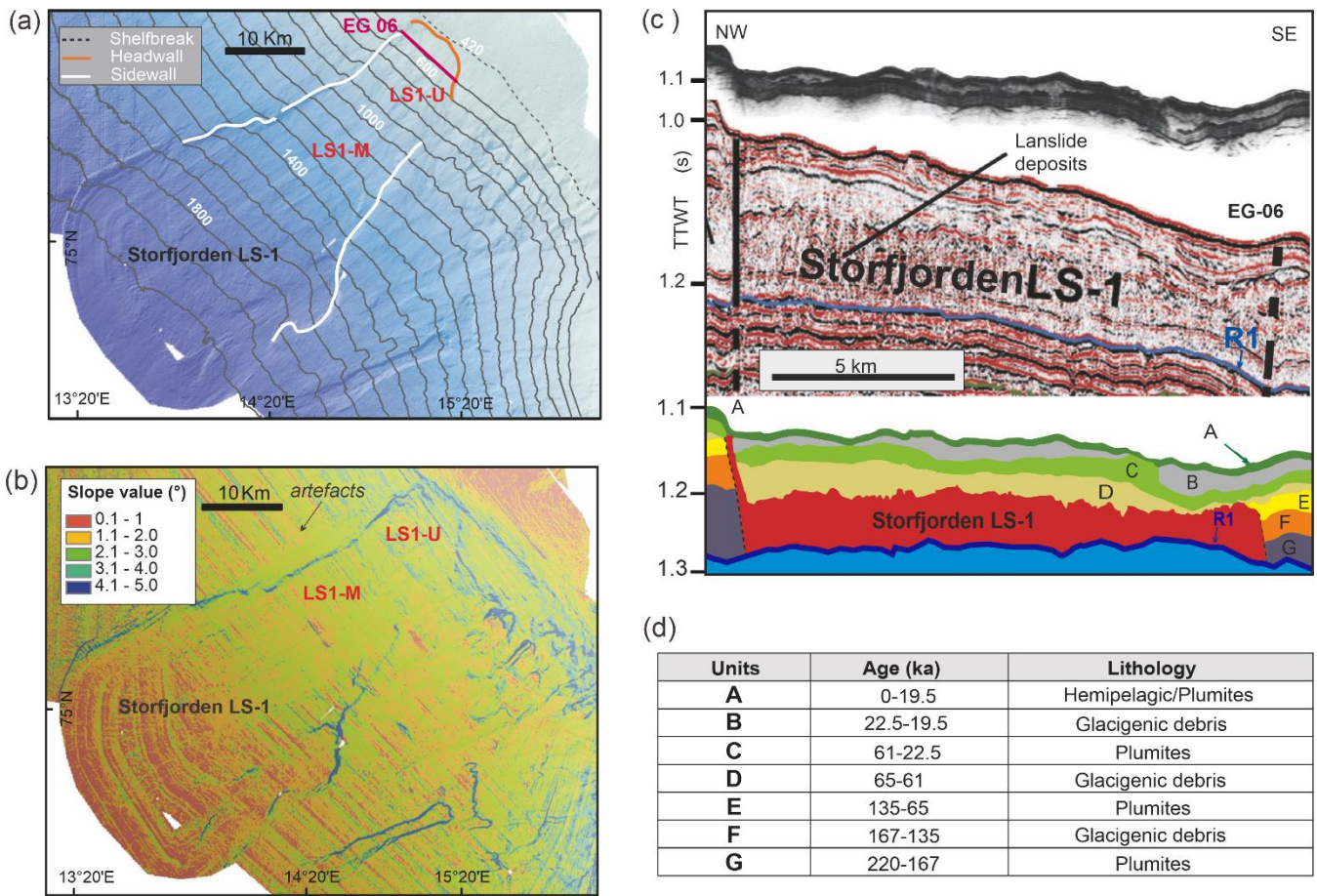
125 **Figure 2.** Shaded relief map from merging the regional data-set (colour map of 250 m; Ottesen, 2006) and high resolution data-sets (grey map of 75 m) of the Storfjorden-Kveithola TMFs, where the Storfjorden LS-1 landslide reaches full data coverage.

3.2. Tsunami numerical modelling

130 The L-ML-HySEA is a mathematical model, which implements a two-phase model to reproduce the interaction between the landslide granular material and the fluid. In the present work, a multilayer non-hydrostatic shallow-water model is considered in order to model the evolution of the ambient water, taking into account dispersive water waves (Fernández-Nieto et al., 2018), and to simulate the kinematics of the Storfjorden LS-1 landslide using the Savage-Hutter model (Eq. 3) (Fernando-Nieto et al., 2008).

135 The L-ML-HySEA model was validated using laboratory experiment data for landslide-generated tsunamis. A milestone in the validation process of this code, consisted in the numerical simulation of the Lituya Bay 1958 mega tsunami with real topo-bathymetric data obtained from González-Vida et al. (2019). The simulation was also used to generate initial conditions for the Method of Splitting Tsunami (MOST), in order to be initialized for the landslide-generated tsunami scenarios of the National Tsunami Hazard Mitigation Program (NTHMP) mandatory benchmarks in the U.S.A. (EDANYA Group, 2015).

140 L-ML-HySEA needs to incorporate the physical properties of the sediment involved in the landslides. In the Storfjorden (SL1) case, properties determined by Lucchi et al. (2013) and Llopart et al. (2019) were used. For the purpose of modelling, we have assumed that the landslide took place in a single event. The simulation has been performed by considering a $\sim 1.3^\circ$ critical slope repose angle, since that value has given the best results across the models.



145

Figure 3. Storfjorden and Kveithola interfan TMFs. (a) Shade relief colour map of the southwestern continental slope of the Storfjorden and Kveithola interfan TMFs. The orange line marks the headwall and the white lines indicate its sidewalls. The red line corresponds with multichannel seismic profile (EG-06) acquired during EGLACOM cruise. (b) Slope gradient values; artefacts are induced by slope parallel the ship tracks. (c) The top corresponds with the TOPAS subbottom profile (modified from Llopart et al., 2015) and multichannel seismic profile (EG-06, modified from Rebesco et al., 2014), acquired during SVAIS cruise. Both profiles are displayed at the same horizontal and vertical scales to show matching of acoustic facies. At the bottom shows the line drawing of the multichannel seismic profile displaying the seismic stratigraphy, where R1 reflector (in blue) is the base of Storfjorden LS-1 and its top is the unit D (Pedrosa et al., 2011; Rebesco et al., 2014; Llopart et al., 2015). (d) Table with the seismic units and subunits, ages and their lithologies (modified from Llopart et al., 2015).

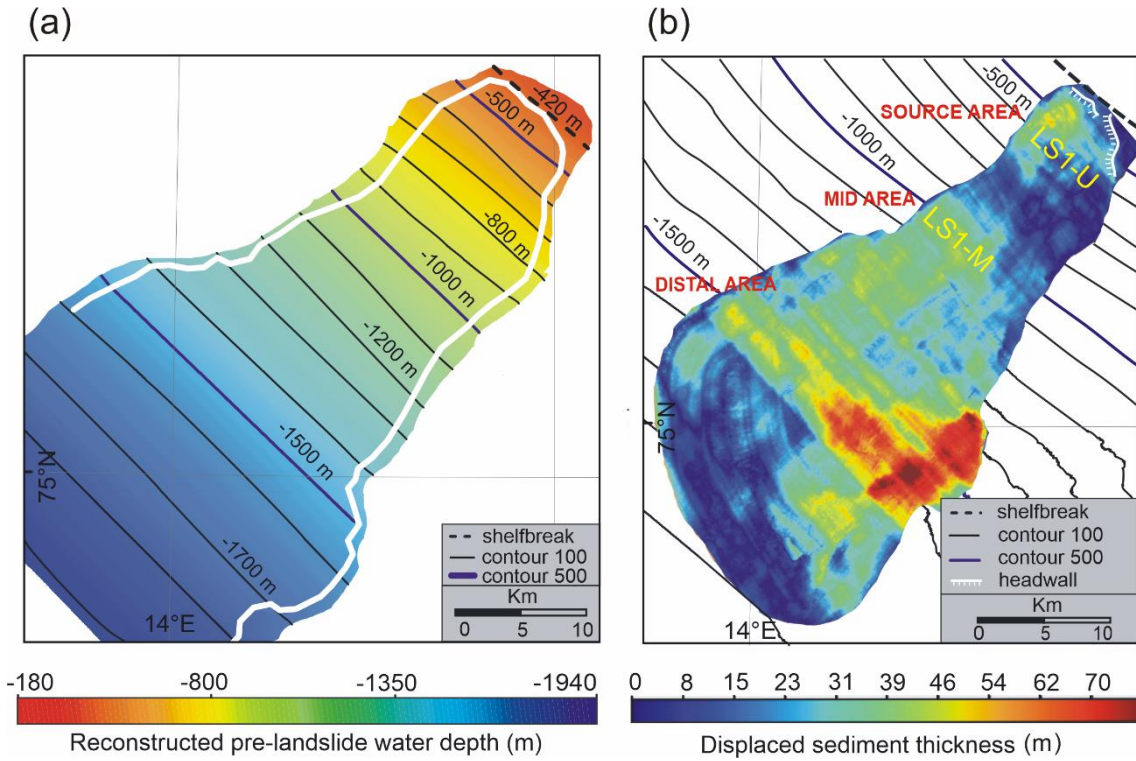
155

3.2.1. Reconstruction of pre-landslide bathymetry and landslide body geometry

160

To perform the L-ML-HySEA numerical simulation, it is necessary to reconstruct the pre-bathymetry before the seafloor failure (Macías et al., 2015). At this aim, we used the high-resolution multibeam bathymetry together with seismic profiles published to define the landslide location, its body geometry, and buried thickness (Pedrosa et al., 2011; Lucchi et al., 2012; Rebesco et al., 2012, 2014; Llopart 2015). We assume that the sedimentary infill thickness 100 ms (Llopart et al., 2015) is roughly similar inside and outside of the landslide, and then, the present-day bathymetry reproduces the pre-Storfjorden LS-1 100 ms difference.

The pre-Storfjorden LS-1 landslide (Fig. 4a) has been calculated by filling the current headwall and lateral scarps areas using the cartographic sewing technique on the bathymetry with B-Splines (Lee et al., 1997), and defining a network of B-spline patches (Eck and Hoppe, 1996). The corresponding control vertices splines were developed using CAD software tools through contour lines from the DEM (Digital Elevation Model) and defined by a tolerance rectangle. When creating the spline, the tolerance rectangle is displayed in the form of construction lines. The control vertices of the rectangle, which are shown as circles, influence the spline curves. The spline is tangent to the tolerance rectangle at the start and end points. In this way, the curve ends up adapting to the hypothetical geometry that best fits each patch. Once the splines were developed, patches were densified through the existing DEM and the points calculated through the splines, generating a new complete DEM without patches. This procedure uses only data points that are not affected by the landslide, and assumes convergence of both data sets (boundary conditions), where the slide scars terminate. A second step involves obtaining the volume of the slid sediment body (Fig. 4b) by calculating the difference between the reconstructed pre and post landslide bathymetry.



180

Figure 4. The Storfjorden LS-1 landslide geometry. (a) Reconstruction of pre-landslide seafloor morphology. (b) Available displaced sediment thickness in meters. Note the location of the different sliding upper and middle sectors (LS1-U and LS1-M, respectively).

185 3.2.2. The L-ML-HySEA model equations and discretization

The Multilayer-HySEA model consists of a two-phase model that represents the interaction between a submarine or subaerial landslide (composed by granular material) and the ambient fluid. A multi-layer non-hydrostatic shallow-water model, (1) was used for modelling the evolution of the ambient water (see Fernández- Nieto et al., 2018), and the Savage-Hutter model was used for simulating the kinematics of the submarine landslide (2).

190

$$S - W \text{ system} \begin{cases} \partial_t h + \partial_x(hu) = 0, \\ \partial_t(hu) + \partial_x\left(hu^2 + \frac{1}{2}gh^2\right) - gh\partial_x(H - z_s) = n_a(u_s - u), \end{cases} \quad (1)$$

$$S - H \text{ system} \begin{cases} \partial_t z_s + \partial_x(z_s u_s) = 0, \\ \partial_t(z_s u_s) + \partial_x\left(z_s u_s^2 + \frac{1}{2}g(1-r)z_s^2\right) - g(1-r)z_s \partial_x H = -r n_a(u_s - u) + \tau_p. \end{cases} \quad (2)$$

195 Here, g is the gravity acceleration ($g = 9.81 \text{ m/s}^2$); $H(x)$ is the non-erodible bathymetry measured from a predetermined reference level; $z_s(x, t)$ denotes the thickness of the layer of granular material at each point x at time t ; $h(x, t)$ is the total water depth; $\eta(x, t)$ represents the free surface (measured from the same aforementioned fixed reference level) and is given by $\eta = h + z_s - H$. $u(x, t)$ and $u_s(x, t)$ are the averaged horizontal velocity for the water and for the granular material, respectively, and $r = \frac{\rho_1}{\rho_2}$ is the ratio of densities between the ambient fluid and the granular material. The friction
200 between the fluid and the granular layer is parameterized with the term $n_a(u_s - u)$. Finally, $\tau_p(x, t)$ represents the friction between the granular slide and the non-erodible bottom surface. The parameterization follows the system proposed in Pouliquen and Forterre (2002).

These two models are coupled through the boundary conditions at their interface. The parameter r represents the ratio of densities between the ambient fluid and the granular material (slide liquefaction parameter).

205 Usually, it is formulated that

$$r = \frac{\rho_f}{\rho_b}, \rho_b = (1 - \varphi)\rho_s + \varphi\rho_f, \quad (3)$$

where ρ_s represents the typical density of the granular material and ρ_f is the density of the fluid ($\rho_s > \rho_f$), both considered constant, and φ represents the porosity ($0 \leq \varphi < 1$). In this model φ is supposed to be constant in space and time and, consequently, the ratio r is also constant. This ratio, r , ranges from 0 to 1 (i.e. $0 < r < 1$) and is a value difficult to
210 estimate even in a uniform material, as it depends on the porosity (and ρ_f and ρ_s are also supposed constant) (Fig. 5).

3.2.2.1. The fluid model

The ambient fluid is modelled by a multi-layer non-hydrostatic shallow-water system (Férendez-Nieto et al., 2018), so that
215 dispersive water waves can be taken into account. The model is obtained by a process of depth-averaging of the Euler equations, and can be interpreted as a semi-discretization with respect to the vertical coordinate.

The total pressure is decomposed into the sum of hydrostatic and non-hydrostatic components, in order to take into account dispersive effects. In this process, the horizontal and vertical velocities are supposed to have constant vertical profiles. The resulting multi-layer model admits an exact energy balance, and when the number of layers increases, the linear dispersion
220 relation of the linear model converges to the same of Airy's theory. Finally, the model proposed in (Férendez-Nieto et al., 2018) can be written in compact form as:

$$\begin{aligned}
\{\partial_t h + \partial_x(hu) = 0, \partial_t(hu_\alpha) + \partial_x\left(hu_\alpha^2 + \frac{1}{2}gh^2\right) - gh\partial_x(H - z_s) + u_{\alpha+1/2}\Gamma_{\alpha+1/2} - u_{\alpha-1/2}\Gamma_{\alpha-1/2} \\
= -h(\partial_x p_\alpha + \sigma_\alpha \partial_z p_\alpha) - \tau_\alpha \partial_t(hw_\alpha) + \partial_x(hu_\alpha w_\alpha) + w_{\alpha+1/2}\Gamma_{\alpha+1/2} - w_{\alpha-1/2}\Gamma_{\alpha-1/2} \\
= -h\partial_z p_\alpha, \partial_x u_{\alpha-1/2} + \sigma_{\alpha-1/2} \partial_z u_{\alpha-1/2} + \partial_z w_{\alpha-1/2} = 0,
\end{aligned}$$

225

(4)

(4)

for $\alpha \in \{1, 2, \dots, L\}$, with L the number of layers and where the following notation has been used:

$$f_{\alpha+1/2} = \frac{1}{2}(f_{\alpha+1} + f_\alpha), \partial_z f_{\alpha+1/2} = \frac{1}{h\Delta s}(f_{\alpha+1} - f_\alpha),$$

where f denotes one of the generic variables of the system, i.e., u, w and p ; $\Delta s = 1/L$ and,

$$\sigma_\alpha = \partial_x(H - z_s - h\Delta s(\alpha - 1/2)), \sigma_{\alpha-1/2} = \partial_x(H - z_s - h\Delta s(\alpha - 1)).$$

230

Schematic picture of model configuration, where the total water height h is decomposed along the vertical axis into $L \geq 1$ layers, (Fig. 5). The depth-averaged velocities in the x and z directions are written as u_α and w_α , respectively. The non-hydrostatic pressure at the interface $z_{\alpha+1/2}$ is denoted by $p_{\alpha+1/2}$. The free surface elevation measured from a fixed reference level (for example the still-water level or mean level in the ocean) is written as η and $\eta = h - H + z_s$, where again $H(x)$ is the unchanged non-erodible bathymetry measured from the same fixed reference level. $\tau_\alpha = 0$, for $\alpha > 1$ and τ_1 is given by

$$\tau_1 = \tau_b - n_\alpha(u_s - u_1),$$

where τ_b stands for a classical Manning-type parameterization for the bottom shear stress and, in this model, is given by

$$\tau_b = gh \frac{n^2}{h^{4/3}} u_1 \nabla u_1 \nabla,$$

240

and $n_\alpha(u_s - u_1)$ accounts for the friction between the fluid and the granular layer. The latest two terms are only present at the lowest layer ($\alpha = 1$). Finally, for $\alpha = 1, \dots, L - 1$, $\Gamma_{\alpha+1/2}$ parameterizes the mass transfer across interfaces, and those terms are defined by

$$\Gamma_{\alpha+1/2} = \sum_{\beta=\alpha+1}^L \partial_x(h\Delta s(u_\beta - \bar{u})), \bar{u} = \sum_{\alpha=1}^L \Delta s u_\alpha$$

Here, we suppose that $\Gamma_{1/2} = \Gamma_{L+1/2} = 0$, which means that there is no mass transfer through the sea-floor or the water free-surface. To close the system, the boundary condition

$$p_{L+1/2} = 0,$$

is imposed at the free surface, and the boundary conditions

$$u_0 = 0, w_0 = -\partial_t(H - z_s),$$

are imposed at the bottom. The last two conditions enter into the incompressibility relation for the lowest layer ($\alpha = 1$), given by

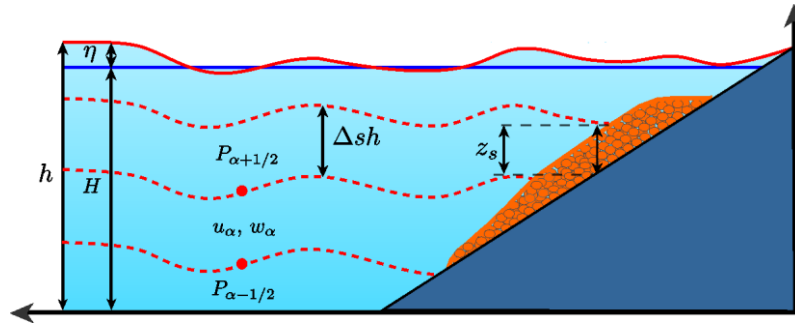
250

$$\partial_x u_{1/2} + \sigma_{1/2} \partial_z u_{1/2} + \partial_z w_{1/2} = 0.$$

It is to be noted that the hydrodynamic model described here and the morphodynamic model described in the next subsection, are coupled through the unknown z_s , that, in the case of the model described here, it is present in the equations and in the boundary condition ($w_0 = -\partial_t(H - z_s)$).

255 Some dispersive properties of the system (4) were originally studied in (Férrandez-Nieto et al., 2018). Moreover, for a better-detailed study on the dispersion relation (such as ‘phase velocity’, ‘group velocity’, and ‘linear shoaling’) the reader is referred to the work of Macías et al. (2020).

260 Along the derivation of the hydrodynamic model presented here, the rigid-lid assumption for the free surface of the ambient fluid was adopted. Therefore, pressure variations induced by the fluctuation on the free surface of the ambient fluid over the landslide are neglected.



265 **Figure 5.** Schematic figure to describe the multilayer system, where water height (h), unchanged non-erodible bathymetry (H), depth averaged velocity in the x direction (u_α), depth averaged velocity in the z direction (w_α), sediment thickness (Z_s), non-hydrostatic pressure at the interface ($P_{\alpha - 1/2}$), free surface elevation measured from a fixed reference level (η), number of layers (L).

3.2.2.2. The landslide model

270 The 1D Savage-Hutter method implemented in the model is given by the system (2). The friction law τ_p (Pouliquen and Forterre, 2002) is given by the expression,

$$\tau_p = -g(1 - r)\mu z_s \frac{u_s^2}{u_s v},$$

275 where μ is a constant friction coefficient with a fundamental role, because it controls the movement of the landslide. Usually, μ is given by the Coulomb friction law as it is the simplest parameterization that can be used in landslide models. However, it is well known that a constant friction coefficient does not allow models to reproduce the steady uniform flows over rough beds that are observed in the laboratory for a range of inclination angles. In the work of Pouliquen and Forterre

(2002), in order to reproduce these flows, the authors introduced an empirical friction coefficient μ that depends on the norm of the mean velocity u_s , on the thickness z_s of the granular layer, and on the Froude number $Fr = \frac{u_s}{\sqrt{g z_s}}$. The friction law is given by:

$$\mu(z_s, u_s) = \begin{cases} \mu_{start}(z_s) + \left(\frac{Fr}{\beta}\right)^\gamma (\mu_{stop}(z_s) - \mu_{start}(z_s)), & \text{for } Fr < \beta, \\ \mu_{stop}(z_s), & \text{for } \beta \leq Fr, \end{cases}$$

with

$$\mu_{start}(z_s) = \tan(\delta_3) + (\tan(\delta_2) - \tan(\delta_1)) \exp\left(\frac{-z_s}{d_s}\right)$$

$$\mu_{stop}(z_s) = \tan(\delta_1) + (\tan(\delta_2) - \tan(\delta_1)) \exp\left(\frac{-z_s \beta}{d_s Fr}\right)$$

where d_s represents the mean size of the grains. $\beta = 0.136$ and $\gamma = 10^{-3}$ are empirical parameters. $\tan(\delta_1), \tan(\delta_2)$ are the characteristic angles of the material, and $\tan(\delta_3)$ is another friction angle related to the behavior when starting from rest. This law has been widely used in the literature (see for instance Brunet et al., 2017).

It is important to remark that this slide model can also be adapted to simulate subaerial landslides. The presence of the term $(1 - r)$, in the definition of the Pouliquen-Folterre friction law, is due to the buoyancy effects, which must be taken into account only in the case that the granular material layer is submerged in the fluid. Otherwise, this term must be replaced by 1 in order to consider subaerial landslides.

In Macias et al. (2021) the reader can find the details about the numerical algorithms used to implement the model. The discretization of the resulting systems is difficult. For the hydrostatic systems that are expressed as non-conservative hyperbolic systems, the natural extension of the numerical schemes proposed in Escalante et al. (2018, 2019) has been adopted, and then solved using a second order HLL (Harten-Lax-van Leer), positive-preserving, well-balanced, path-conservative finite-volume numerical scheme (see Castro and Fernandez-Nieto, 2012). Then, the non-hydrostatic pressure corrections at the vertical interfaces required the discretization of an elliptic operator, and that was done using standard second-order central finite differences. This resulted in a linear system that was solved using an iterative scheduled

Jacobi method. Finally, the computed non-hydrostatic corrections were used to update the horizontal and vertical momentum equations at each layer, and, at the same time, the frictions were also discretized (see Escalante et al., 2018, 2019). For the discretization of the Coulomb friction term, the procedures presented in Fernández-Nieto et al. (2008) were followed.

The resulting 2D numerical scheme is well balanced for the water at rest stationary solution and is L^∞ stable under the normal CFL condition. The scheme is also positive preserving; that means that the thickness of the water layer will be always positive or zero, but never negative and can be used with emerging topographies.

For dealing with numerical experiments in 2D regions, the computational domain must be decomposed into cells, or finite volumes with a simple geometry. Here, a Cartesian type UTM was used. The 2D numerical algorithm for the hydrodynamic hyperbolic component of the coupled system is well suited to be parallelized and implemented in GPU architectures, as is

shown in Castro et al (2011). Unfortunately, the standard treatment of the elliptic part of the system is not compatible with the parallelization of the algorithms. However, in Escalante et al. (2018, 2019), a multi-GPU implementation was presented and made possible because of the compactness of the numerical stencil, and the massive parallelization of the Jacobi method. Such a multi-GPU implementation of the complete algorithm results in much shorter computational times, and that is the reason why it was used in this work.

4 Results

315

4.1. The Storfjorden LS-1 landslide geometry

The Storfjorden LS1 landslide is ~ 60 km in length and covers an area of more than 1300 km² (Llopart et al 2015). Three main morphological elements are imaged by the multibeam bathymetry: headwall, sidewalls and sliding area (Fig. 3a). The headwall displays a well-defined seaward-concave scarp that forms an amphitheatre-like feature about 12 km long and > 50 m in relief. Its slide scar is incised into the shelf-edge at 420-480 m water depth. The northwestern sidewall is defined by a striking 25 km long scarp, 35-40 m in relief, and with a rectilinear to slightly sinuous pathway. The southeastern sidewall occupies 35 km long with 25 to 80 m of relief, representing the highest in the mid area (~1500 m water depth). The width between the sidewalls is variable downslope. The sidewalls are roughly parallel and define a bottle neck shape of 18 km wide, down at ~1330 m water depth, which increases to 32 km at ~1900 m water depth. The sliding area displays an elongated lobate shape, in plan-view, with an irregular seafloor. The seafloor gradients are typically 2° to 3° at ~1330 m water depth, and < 2° toward the distal ends, (Fig. 3b). The chaotic landslide deposits in the upper slope (800 m depth) is shows in the Fig. 3c, (Llopart et al., 2015).

325

4.2. Submarine landslide and tsunami numerical simulations

330

The numerical simulation consists of several successive steps aimed at reconstructing: i) the smooth pre-landslide upper slope and landslide body geometry following the methods described in section 3.2.1 (Fig. 4); ii) the landslide dynamic (Fig. 6); iii) the tsunami wave generation (Fig. 7); and iv) the tsunami wave propagation and its impacts on the coast (Figs. 8 and 9).

4.2.1. Modelling the landslide dynamic

335

Once the smooth pre-landslide upper slope had been calculated, following the methods described in section 3.2.1 (Fig. 4), the landslide body geometry was determined. The numerical landslide rupture simulation begins with the slope failure of the Storfjorden LS-1, which assumes that it fails at once and moves downslope by gravitational forces (Macias et al., 2016). Conventional studies about submarine slides show the difficulty in assessing whether their occurrence represents unique events

340

(Casas et al., 2016; Chiocci and Casalbore, 2017; Vázquez et al., 2022). The morphological results would also support that assumption for the Storfjorden LS-1, due to the lack of retrogressive structures, which would point to a decrease in the tsunamigenic potential (Harbitz et al., 2006). A few local and small-scale slope failures seem to occur on the southeastern flank in the mid slope (~1600 m deep), but they wouldn't be significant in the modelling of the main landslide event, due to its low potential to transfer deformation to the water column.

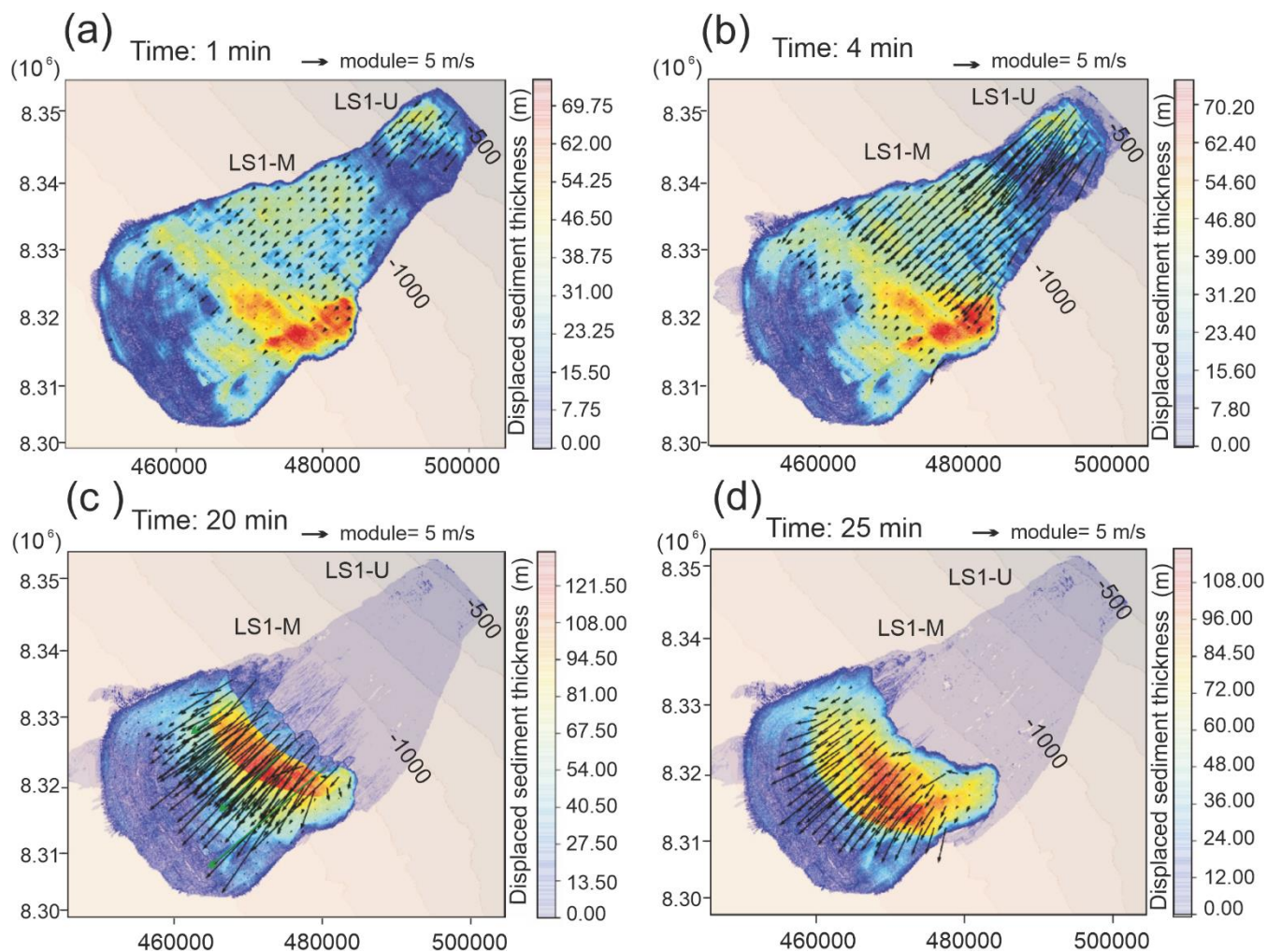
In addition, by comparison with similar deposits from other continental slopes (Iglesias et al., 2012; Casas et al., 2013; Casas et al., 2017; Vanneste et al., 2006; Winkelmann et al., 2008), the Storfjorden LS-1 shows a well-defined arcuate slide scar, mostly rectilinear side walls, and a cutting basal shear surface. Its moving mass defines a subtabular body with chaotic deposits, and without apparent internal discontinuities that sharply interrupt the lateral continuity of the surrounding deposits (Pedrosa et al., 2011; Lucchi et al., 2012). All these characteristics put together tentatively point to a single sliding process, not being demonstrated as multiple failure in the previous literature (Pedrosa et al., 2011; Lucchi et al., 2012; Rebesco et al., 2012, 2013). The difference between pre- and post-landslide bathymetries is 40 km³, a volume that was comprised between 33 km³ proposed by Pedrosa et al. (2011) and the 46 km³ by Llopart et al. (2015). The numerical landslide rupture simulation shows that the moving mass was comprised of two domains with different behaviour, based on the velocity pattern (Fig. 6a, 6b). At 1 min after slide, an upper slope domain (LS1-U, ~500 m water depth, ~3° slope gradients) is related to the moving sediment nearest to the slide scar and moves faster ($v_u=5$ m/s) than middle slope domain (LS1-M, ~1000 m water depth; 2° slope gradients, $v_m=1$ m/s) (Fig. 6a and 7, steps 1; suppl. video 1). At 4 min, the velocity increases in the upper slope domain $v_u=30$ m/s and in the mid slope domain $v_m=22$ m/s (Fig. 6 and 7, step 2; suppl. video 1). At 20 min, the sliding velocity maximum in the frontal area is $v_f=20$ m/s and decreases gradually towards the sides of slide with values around $v_s=15$ m/s (Fig. 6c, and 7, step 10 and suppl. video 1). At 25 min, the sediment sliding became homogeneous in the distal area (~1500 m water depth). The velocity decreases gradually downslope, where the frontal area of sediment sliding velocities reach around $v_f=10$ m/s and in distal area $v_s=2-5$ m/s.

The landslide characteristics modelled by L-ML-HySEA determine an average velocity (v_a) =25 m/s, a terminal time (t_t) of ~ 40 min, and a characteristic distance (d_c) of at least ~ 60 km.

Landslide geometry	V (km ³)	40
X ₁ S11-upper slope (m E)	490000	
Y ₁ S11-upper slope (m N)	8350000	
X ₂ S11-middle slope (m E)	485000	
Y ₂ S11-middle slope (m N)	8340000	
h (m)	420	
l (km)	60	
w (km)	8	
T _p (m)	35	

	T_d (m)	122
	A_z (°)	N225°E
	Θ (°)	2°
Landslide dynamics	v_u (m/s) at 1 min	5 m/s
	v_u (m/s) at 1 min	30 m/s 370
	v_m (m/s) at 4 min	1 m/s
	v_m (m/s) at 5 min	22 m/s
	v_f (m/s) at 20 min	15 m/s
	v_f (m/s) at 25 min	10 m/s
	v_s (m/s) at 20 min	15 m/s
	v_s (m/s) at 25 min	2-5 m/s 375
	V_t (m/s)	25 m/s
	t_t (s)	~ 2400
	d_c (km)	~ 60
Initial tsunami	C_i (m)	0.3
	v_{ta} (m/s)	136
	v_r (m/s)	81 380
	v_n (m/s)	46.6
	v_e (m/s)	51.6

Table 1.Storfjorden LS-1 geometry and mechanical characteristics. The inputs for the model are related to the landslide geometry: the total volume (V); the longitude and latitude of the submarine landslide relative to the LS1-Upper slope area (X_1 , Y_1), and in the LS1-Mid slope area (X_2 , Y_2); the initial depth (h) before the slope failure; the length (l) (long axis) and width (w) (small axis); the maximum thickness in proximal and distal (T_p and T_d respectively); the mean azimuth direction of landslide (A_z); the mean slope gradient (Θ). The outputs of model are related to the landslide dynamic: velocities to the landslide in the upper-slope (v_u) and the landslide located in the mid-slope (v_m); sliding sediment in the frontal area (v_f); sliding sediment in the sides (v_d); total velocity (v_t); terminal duration (t_t); and characteristic distance (d_c). The outputs related with initial tsunamis: wave crest (C_i) tsunami velocity at 1900 depth (v_{ts}); tsunami waves velocity during refraction (v_r), tsunami waves velocity toward northern (v_n), tsunami waves velocity toward southeastern (v_e).



395

400

405

Figure 6. Velocity pattern of landslide in different frames and the displaced sediment thickness. (a) 1-min frame, in where upper slope domain (LS1-U, ~500 m water depth, 3° slope gradient) with average velocity is $v_u=5$ m/s contrast versus the mid slope domain (LS1-M, ~1000 m water depth; 2° slope gradients) with velocity average $v_m=1$ m/s. (b) 4-min frame, with a progressive velocity increase in both areas ($v_u=30$ m/s and $v_m=22$ m/s respectively). (c) 20-min frame, velocity is maximum in the frontal area $v_f=20$ m/s that coincided with maximum sediment thickness displaced (122-108 m) and decreasing towards the sides $v_s=15$ m/s. (d) 25-min frame, both moving masses are joined with central velocity $v_f=10$ m/s and lateral $v_s=2-5$ m/s in distal area (~1500 m water depth).

4.2.2. Tsunami wave generation

410 Free water surface changes at any point along the time are determined according to seafloor deformation (Fig. 7 and suppl. video 1). In the initial stage (4 to 5 min), the tsunami wave has two NW-SE trending dipoles, LS1-U, smaller (25 km long) and more striking, and LS1-M, larger (35 km long) and smoother. They have been created by the water-mass infilling the empty spaces produced by the sudden evacuations and uplifting of fast downslope moving mass. Both wave dipoles have the troughs at shallower waters (~600 to 800 m) than their respective crests (~700 to 1000 m water depth) (Fig 7 step 1 and 8).
415 The synthetic marigram on the upper slope (station 1) of the Storfjorden LS-1 (Fig. 9a, b and c) highlights the initial wave generation with the crest and trough well defined, registering a crest amplitude value of 0.4 m (above LS1-U) and a trough amplitude value of up to 1.1 m at 3 min, followed by a crest amplitude value of 0.3 m (Figs. 8 step 1, 9b and suppl. video 2).

After 3 min, the two initial dipoles evolve into a single NW-SE trending dipole (crest amplitude value of 0.3 m), whose trough (0.5 m) is, also at shallower waters (~1000 m) than the crest (~800 m) (Figs. 7 step 3, and 8 step 1). Wave rebound occurs (Fig. 7, step 4 to 9) when a maximum amplitude of ~2.7 m is registered over the distal area of the landslide (Fig. 9c, station 2, and suppl. video 2). At 7 to 9 minutes, a new crest wave amplitude value of 0.5 m appears parallel to the single dipole (Fig. 7, step 4 to 5 and suppl. video 1) at shallower waters (1400 m). It enlarges with time up to 0.7 m, whereas the trough largely keeps its dimensions or relief. At the 16 min mark, the tsunami wave reaches the highest amplitude (at 1780 m water depth), with a trough amplitude value of 2 m and a crest amplitude value of 0.7 m (Fig. 9, station 2).

425 At minute 25, the tsunami wave evolves into a larger dipole above the landslide, opposite to the first ones, with a trough amplitude value of 0.5 m and a crest amplitude value of 0.3 m (at 1200 m water depth). This dipole gets smaller with time, and a crest amplitude value of 0.5 m at shallower waters (900 m water depth) covering large areas with time (Fig. 7, step 10).

4.2.3. Tsunami wave propagation and coastal impact

430 The tsunami wave dynamics are illustrated by the maps of the wave height across time (Fig. 8 and suppl. videos 1 and 2). Synthetic marigrams have been included at key locations in order to highlight the wave propagation and coastal impact in: the northwestern flank of Spitsbergen Bank (Fig. 9d, station 3); the onshore of Kveithola glacial trough (Fig. 9e, station 4); the Spitsbergen Bank (Fig. 9f, station 5); the onshore northern boundary of mid-shelf of Storfjorden glacial trough (Fig. 9g, station
435 7); and the onshore southwestern Spitsbergen coast (Fig. 9h and 9i, stations 7 to 8).

The initial tsunami wave starts propagating from the landslide area with a trough wave moving northeast towards the coast, and a crest wave moving southwest (Fig. 8, step 3 and suppl. videos 1 and 2). The tsunami waves propagate elliptically, with crest and trough elongated in the NW-SE direction (Fig. 7, step 3) and total velocity (v_{ts}) of ~136 m/s. During the tsunami propagation from depth value (~1900 m) towards shallow water (~250 m) (Fig. 8 and suppl. video 2), the refraction phenomenon occurs during shoaling. The synthetic marigram records the refraction clearly due to an irregular variation in the general amplitude pattern (Fig. 9d, station 3). Refraction effects in a wave front show a decrease in velocity down to ($v_r=$ 81

m/s) and an increase in amplitude. The values change from a trough amplitude of 0.25 m to a crest amplitude value of 0.18 m (Fig. 9e, station 4). While the values change from a trough amplitude of 4.2 m to a crest amplitude of 4.3 m (Fig. 9f, station 5). Furthermore, it can be observed that the tsunami propagation front displays a crescent shape.

445

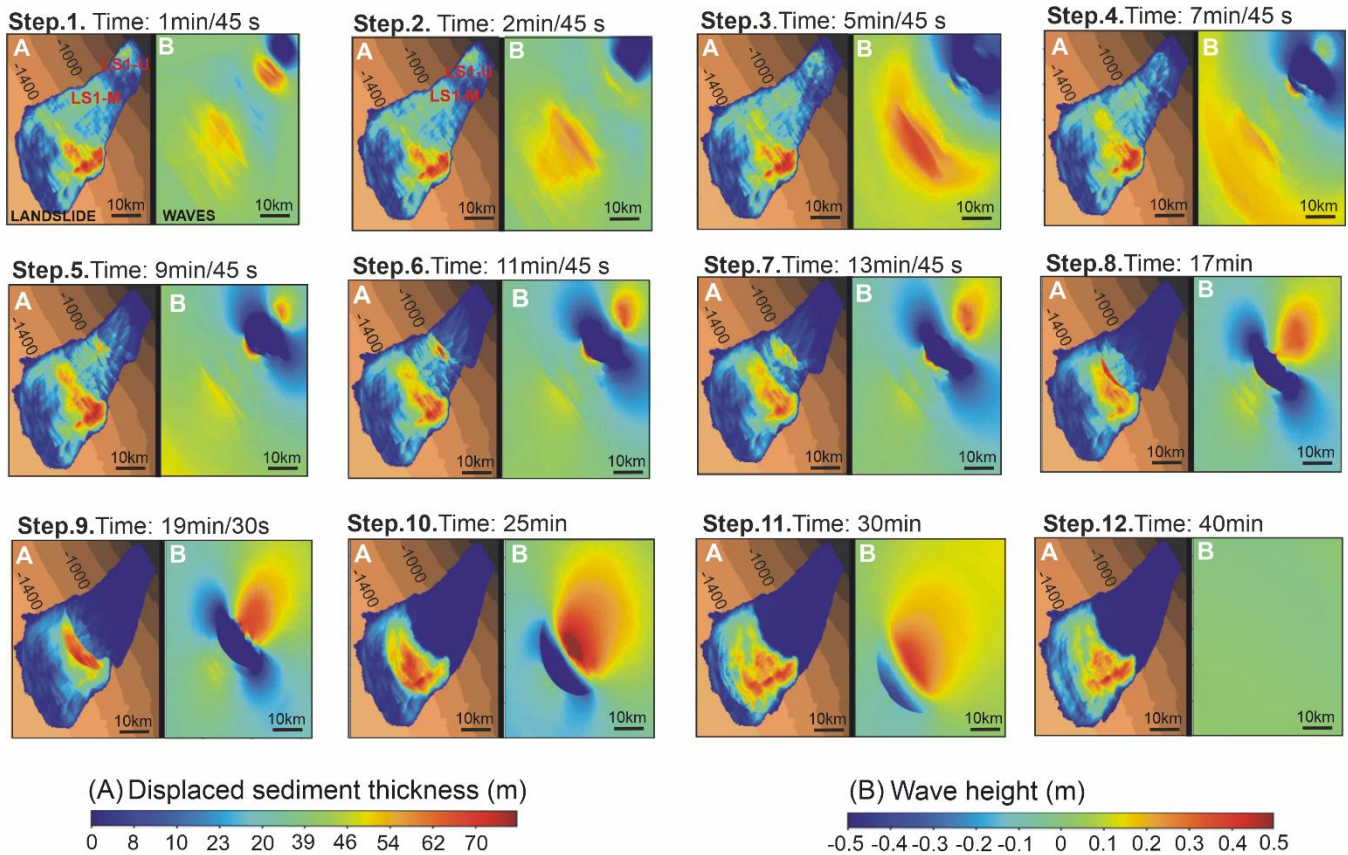
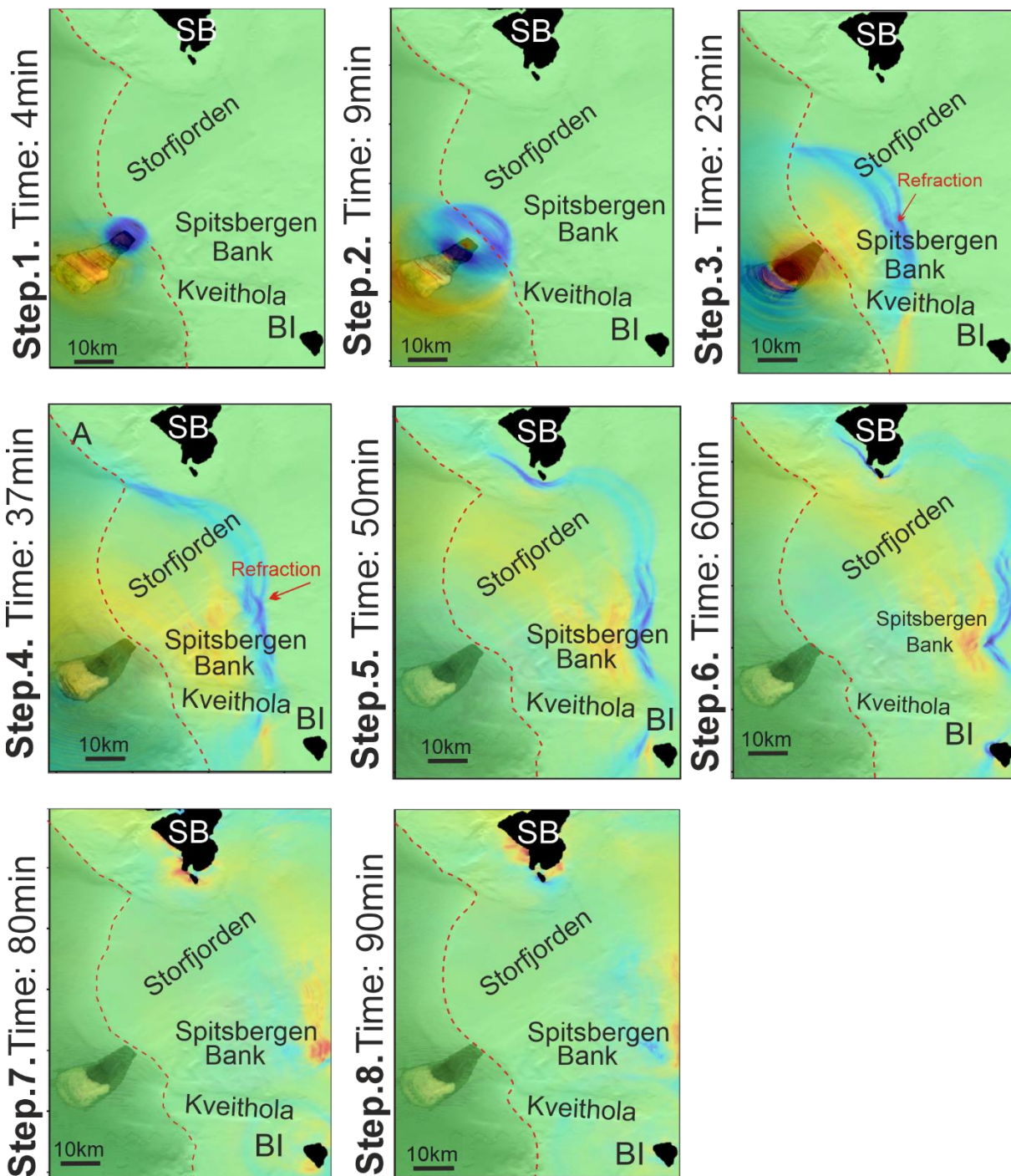


Figure 7. Main composition in twelve consecutive frames. (a) Evolution of the landslide, where can be distinguished two sliding sediment masses in the firsts 25 minutes, one in the upper slope (S11-U) and the other one in the lower slope (SL1-M), which are merged in a unique one at after 25 min. The colour scale corresponds with available sediment thickness to be displaced in meters. (b) Dipole waves evolution of outgoing tsunami with the wave height values.

The tsunami arrival times are observed based on the propagation direction toward the coast. The impact of tsunami waves affects the Sørkappøya at 50 min (southern Spitsbergen), with trough amplitude value of 0.3 m, increasing to a crest amplitude value of 0.2 m at 75 min (Fig. 8 step 5 and 9h). At the same time (50 min), the impact occurs at Kapp Dunnér (northwest Bear Island) with tsunami waves having a crest amplitude value of 0.3 m, at 50 min, which increases to 0.5 m at 53 min (Fig. 8 step

5 and suppl. video 2). After these two first coastal impacts, the tsunami affects different parts of both islands at different times. The southwestern Bear Island is reached by the tsunami waves at 60 min with a maximum crest amplitude value of 0.5 m, (Fig. 8, step 6), followed by a trough amplitude value of 0.5 m at 65 min. Likewise, the north of Bear Island is affected by a trough amplitude value of 0.5 m (Fig. 8, step 6), and a crest amplitude value of 0.5 m at 80 min (Fig. 8, step 7). In the Svalbard, the Stombukta Bay (southwestern Spitsbergen Island) is the next impacted coastline (Fig. 9a). There, the tsunami waves show specific velocity of $v_s=13$ m/s (at 18 m of depth), with trough amplitude values of 0.3 m at 63 min that increases crest amplitude value up to 0.32 m (85 to 95 min) (Fig 8 steps 7 to 8, and 9i). Finally, tsunami wave series propagating toward the coast occur until two hours after the Storfjorden LS-1 landslide triggering (suppl. video 2).



485 **Figure 9.** Synthetic marigrams. (a) The location map of the synthetic marigrams above the reference stations, numbered in
figure (a) (station 1 to 8). Note the different arrival times, periods, wave heights, and polarities at the different stations (b) to
(i).

The submarine landslide geohazard studies are not easy to conduct due to the difficult access that the marine
490 environment imposes, which makes it hard to obtain accurate analysis and monitoring. Our case study suggests that numerical
modelling is of great help in understanding the dynamics of submarine landslide geohazard, and their tsunamigenic potential.
The Storfjorden upper continental slope presents critical conditions that need to be taken into account, and warrants carrying
out studies to assess slope-stability. Several factors support this assertion: (i) the overpressure ratios measured in the subsurface
sediments (Lucchi et al., 2013; Llopart et al., 2019) and (ii) the seismicity related with the active Horsund Fault Zone (Hampel
495 et al., 2009; Auriac et al., 2016; Pirli et al., 2019). In addition, (iii) the recent environmental stress represented by the factors
mentioned above may intensify processes such as gas-hydrate dissociation and fluid flow migration (León et al., 2021). Lastly,
(iv) unloading rebound seismicity during ice retreat/melting (Berndt et al., 2009) also may contribute to trigger new submarine
landslides.

500 **5.1. Landslide dynamics and wave generation**

Key landslide parameters for the generation of tsunamis commonly include volume, velocity and initial acceleration of the
sliding mass (Harbitz et al., 2006; Urlaub et al., 2013; Løvholt et al., 2015; Macias et al., 2015; Urgeles et al., 2018) (Table 1).
In our case study, the relationship between the above mentioned parameters is also fundamental for the formation of a tsunami.
505 The L-ML-HySEA model indicates that the 40 km³ of available displaced sediment volume moved by the Storfjorden LS-1
landslide is enough to trigger a tsunami. The morphosedimentary characteristics of the Storfjorden LS-1 landslide suggest that
mass failure deposits could occur as a single event, as opposed to several, implying a better energy transfer to the water column
(Vázquez et al., 2022 and references therein); therefore, velocity and initial acceleration also would be key for the formation
of the tsunami. In this sense, for the phase velocity to be highly effective at the depths of the Storfjorden LS-1 ($H = 420$ to
510 1900 m) during the tsunami waves onset, its value should be $v_{ta}=136$ m/s (Tinti and Bortolucci, 2000; Fryer et al., 2004). The
relatively average velocity (roughly 25 m/s, Table. 1) obtained for our tsunami indicates that it was out of phase and, therefore,
it would not have been effective enough to create high amplitude tsunami waves (Huggel et al., 2005; Evans et al., 2009;
Pudasaini., 2014; Dietrich and Krautblatter, 2019).

515 Our results indicate that the characteristics of the tsunami wave are influenced by landslide dynamics at two stages
of the downslope moving mass: initial (1 to 4 min) and late (20 to 25 min), with different velocities values (Fig. 6). The two
initial wave dipoles, generated when seafloor failure occurs, are the consequence of two large seafloor depressions, one at the
slide scar (i.e. main evacuation area), and the other one located between the two mass moving domains (Fig. 7, suppl. video

1). At 25 min, a new dipole is formed, opposite to the previous ones. This new dipole is created when the faster sliding mass reaches the slower one, and both masses merge producing a significant impact in the available displaced sediment thickness (100 m) of the distal moving mass. The increase in thickness would contribute to increase the pressure in the water column causing the uplift in the water surface and the enhancement of the tsunami waves (Ramadan et al., 2018; Ercilla et al., 2021). Thus, our study demonstrates that a proper understanding of landslide dynamics at their initial stages (or first motion), and of their deformation during the run-out, are crucial requirements for understanding the characteristics of the initial tsunami waves, and the effects that those characteristics have on their evolution. In addition, our study also suggests that identifying the initial tsunami wave forms could reveal the tsunami sources, e.g. landslides (generating single or multiple trough and crest pairs) *versus* faults (generating a single or crest wave) (e.g., Macias et al., 2016; Ercilla et al., 2021; Estrada et al., 2021; Bécel et al., 2017).

530 **5.2. Seafloor morphology**

It's widely known that how a tsunami wave propagates is highly dependent on the morphology of the seafloor (Urlaub 2013; Estrada et al., 2021). The model shows that tsunami waves propagate elliptically with respect to the NE-SW elongated seafloor shape of the landslide relief. In the Storfjorden SL-1 tsunami, the average velocity waves ($v_{ta}= 136$ m/s) travel northeastern and are focused between the continental shelf of the Svalbard and of Bear Island, which helps to confine it, and forces its direction of propagation (Fig. 8 and suppl. video 2). The continental shelf morphology determines tsunami shoaling, with the shallowest water depths located at the Spitsbergen Bank (80 m water depth). The shoaling by the bank produces the refraction phenomenon and the amplification of the tsunami. As the tsunami propagates across the ocean, waves can undergo refraction, which is caused by segments of the wave moving at different speeds as the water depth along the wave front varies (Berkhoff., 1972; Gangfeng et al., 2012). This effect produces variations in the amplitude of the tsunami waves and in their arrival times: 15 min later at southwestern Spitsbergen and 11 min later at northwestern Bear Island. When encountering an obstacle, the tsunami waves discharge their energy with great force, as in the case of Sørkappøya and Sørkapp at 75 min, decreasing the amplitude and slowing down the arrival time of the tsunami waves in the corresponding bay to 100 min (suppl. video 2). The tsunami waves arrival is recorded at 80 to 95 min at the eastern Hornsund-fjord. On the other hand, the crescent shapes of the tsunami front seem to be conditioned by the Storfjorden and Kveithola glacial troughs separated by the Spitsbergen Bank. The elongated negative reliefs of the glacial troughs would cause the funnelling of the tsunami sea water with relative higher specific velocities of propagation ($v_s=56$ m/s in Storfjorden glacial trough at 320 m water depth). Therefore, the numerical simulations are a useful tool to assess tsunami hazard in places where local seafloor topography could advance or delay the tsunami waves, and therefore the coastal impact.

550 The Storfjorden SL-1 modelling has demonstrated that the shelf seafloor morphology is a decisive factor: it influences the propagation velocity of the tsunami waves, the variations of wave amplitude (shoaling effect), and the impact of coastal arrivals (Iglesias et al., 2012; Estrada et al., 2019; Salaree and Okal, 2022).

5.3. Coastal location

555

The initial tsunami waves start propagating as negative and positive disturbance dipoles. The trough is always located towards the upper part of the margin, which determines that, in general, the first arrival to the coast corresponds to a sea level drop, hence decreasing the coastal impact. This factor, together with coastal location and orientation (i.e., angle of the waves with the coastline), condition the polarities of the first arrival wave. In our study, the first arrival wave impacted with trough values of 0.1 to 0.5 m against the coast of southwestern Spitsbergen, and with crest values of 0.1 to 0.5 m against Bear Island (Fig. 8 and suppl. video 2).

560

5.4. Comparison with other landslide tsunamis: hazard assessment for the northern glaciated margins

565

Landslide parameters (age, area, volume, seafloor gradients, location, and velocity) and related tsunami parameters (wave amplitude, velocity) of different landslide inducing tsunamis have been compared with those defining the Storfjorden LS-1 and its tsunami, in Table 2.

Event	Age (ky)	Area (km ²)	Volume (km ³)	Location	Wave amplitudes	Deposits type	Headwall depth (m) base slope (°)	Trigger	slide velocity (m/s)
Storfjorden LS-1	< 200	1200	40	Storfjorden TMF	2.5 to (proximal) 1.5-8 (distal)	DF	420 to 1900 2° to 3°	A, B	25
Hinlopen	30	2400	1150	Arctic	130 to 40	MW LRB TC	300 12° to 30°	A, B	-
Kongsfjorden TMF	-	9100	500 to 1000	Western Spitsbergen	1.5 to 5.6 (proximal) 0.6-1 (distal)	DF MW	200 3° -10°	A, B	35
Bjornoyrenna	< 300	12500	1100	NW Barents	-	DF	400 2° to 3°	A, B	-
Gebra Valley	100	230	-	Central Bransfield Basin	-	DF	750 to 1930 2° to 1°	A, B	-
Grand Banks	1929	20000	185	Newfoundland	3 to 8 (proximal) 9 to 15 (distal)	TC	500	B	-
Storegga	8.18	95000	2400 to 3200	North Atlantic	15	DF MW	1000	B	-
Trænadjupet	4	-	900	Norway	0.3 to 1	DF MW LRB	400	A, C	-

Nyk	16.3	2200	-	Norway	-	DF MW	1200 to 1600	A, C	-
Skagway	1994	-	0.003	Alaska	13 to 7 (proximal) 1.3 to 0.2 (distal)	-	-	D	-
Lituya Bay	1958		0.31	Alaska	272 to 251 (proximal)	-	-	D	110
Big'95	11.5	2200	26	Western Mediterranean	8 to 6 (proximal) 4 to 2 (distal)	DF	200 to 1800	A, B	50

570 **Table 2.** Submarine landslides compared with Storfjorden LS-1. In the triggers column the letters represent: (A) Weak-layer
Sedimentary Architecture, (B) Earthquake, (C) Gas Hydrate Dissociation, (D) Other additional factors. Deposits type: mass
wasting (MW); large rafted blocks (LRB); turbidity currents (TC); debris flows (DF); slump blocks (SB). References:
Storfjorden LS-1 (Pedrosa et al., 2011; Lucchi et al., 2012; Rebesco et al., 2014; Llopart et al., 2015); Hinlopen (Winkelmann
et al., 2008; Vanneste et al., 2006); Bjornoyrenna (Laberg et al., 1999); Gebra Valley (Garcia et al., 2008, Casas et al., 2013)
575 Grand Banks (Piper et al., 1999; Fine et al., 2005); Storegga (Haflidason et al., 2004; Bondevik et al., 2012); Kongsfjorden
TMF (Bernt et al., 2009); Trænadjupet (Laberg et al., 2002b); Nyk (Lindberg and Laberg., 2004); Skagway (Thomson et al.,
2001; Synolakis et al., 2002); Lituya-Bay (González-Vida et al., 2019); Big'95 (Iglesias et al., 2012).

This comparison highlights that not only large, but also relatively small-medium sized landslides, could have triggered
580 tsunamis in the past. Despite the Storfjorden LS-1 having a smaller area and volume with respect to the larger landslides of
the Kongsfjorden TMF, the amplitude value of their respective tsunami waves is roughly similar. The effects of global warming
over the landslide triggering factors (e.g., isostatic rebound seismicity and gas hydrate destabilization by the rise in temperature
of the ocean water) is not likely to provoke the occurrence of such large landslides as those formed during glacial maxima and
the transition from glacial to interglacial periods (Lee, 2009 and references therein). However, the present trend of global
585 warning should over time increase the probability of slope instability, especially on those glaciated margins that have not yet
failed after the last glacial to interglacial transition, for instance: the Bear Island Trough Mouth Fan , Kongsfjorden Trough
Mouth Fan and Storfjorden TMF (Bergnt et al., 2009). Therefore, the results presented here should encourage us to continue
working in the prediction of tsunamigenic landslide hazards and their coastal impact, mainly in the northern glaciated margins.

590 The water depth location of the landslide scar seems to influence the coastal impact of tsunami waves (Table 2). In the
study area, they present low amplitude values at the coastal area and their arrival times are longer (50 to 80 min) than the
tsunamis modelled in the nearby coast of western Spitsbergen (Bernt et al., 2009), where the slope failure is at shallower water
depths (200 m) and the distance to the nearby coast is shorter (~ 90 km). Landslides triggered at shallower water result in more
localized waves, and the elongated landslide velocity profile delays the appearance of the first positive landward propagating

595 wave, hence reducing the chances of constructive interference along the coast (Harbitz et al., 2006). This suggests that tsunami
modelling based on past landslides should pay more attention to those sectors of the northern glaciated margins with narrower
continental shelves and submarine landslide head scarps that are near the shoreline. The landslides located in the middle and
northern parts of Norway are a good example of that (L'Heureux et al., 2011; Beaten et al., 2013). Also, much smaller collapses,
either submarine or subaerial, also pose a significant local threat. In Norway, several rockslide tsunamis occurred in the 20th
600 century, the most devastating in Storfjorden in 1934 (Blikra et al., 2005; Böhme et al., 2015). Although this is not the scope of
the paper, they could be more frequent with estimated rate 1 event per 1000 years (Blikra et al., 2005).

In summary, our findings demonstrate that tsunami modelling based on past landslides using the L-ML-HySEA
landslide tsunami model will be useful to provide new perspectives on tsunami hazard assessment in polar margins, where
605 global climatic change and its related ocean warming may contribute to the activation of landslides. Landslide tsunami models
will allow us to identify the areas with maximum and faster coastal impact, and the effect of the local bathymetry on tsunami
direction of propagation, shoaling, amplification and diffraction. This knowledge is very important for the design of early
warning strategies, as it will contribute to assess the key factors that are useful as emergency planning tools.

610

Code availability.

The source code of SVAIS and EGLACOM projects used in this study is available from
<https://sites.google.com/site/ipynicestreams/home>

615

Data availability.

Video Supplement

620

video1: <https://av.tib.eu/media/56981>

video2: <https://av.tib.eu/media/56982>

625 *Author contributions*

M.P., J.G. and G.E conceived the idea for the study and wrote the paper with methodological contributions from J.G.V. in the
tsunami mathematical model and S.O. and in the seafloor deformation and the tsunami potential. The geodynamic framework

was done by M.T, J.G. and G.E. Seismic data compilation and the figures were done by M.T. In the same manner D.C.
630 contributed in the discussion. The propagation tsunami model was done by J.G.V., S.O. and M.C. as well as associated videos.
All authors provided guidance on the analyses and commented on the manuscript.

Competing interests.

635 The authors declare that they have no conflict of interest.

Acknowledgments.

We thank Prof Sakellariou and Dr. Casalbore for their helpful comments and discussion. This research was supported by
640 Spanish IPY projects SVAIS (POL2006-07390/CGL) and IPY-NICE STREAMS (CTM2009-06370-E/ANT). Also, the
research group, RNM 148, and projects PAPEL B-RNM-301-UGR18 and AGORA P18-RT-3275 (Junta de Andalucía) and
project GOLETA PID2019-108880RJ-I00 / AEI / 10.13039/501100011033. We would like to thank the EDANYA research
group from University of Malaga and also Javier Valencia. In addition, all scientists and crew who participated in seagoing
activities to obtain geophysical data in the framework of SVAIS cruise. We are grateful to Dag Ottesen (NGU) for providing
645 the Norwegian Hydrographic Service Bathymetry. The authors wish to acknowledge the cooperation of Captain Pedro Luis de
la Puente García-Ganges (*BIO Hespérides*), and of the technical staff at the UTM (CSIC, Barcelona). This work represents a
contribution to CSIC Thematic Interdisciplinary Platform PTI POLARCSIC.

References

- 650 Auriac, A., Whitehouse, P. L., Bentley, M. J., Patton, H., Lloyd, J. M., and Hubbard, A.: Glacial isostatic adjustment associated
with the Barents Sea ice sheet: a modelling inter-comparison, *Quat. Sci. Rev.*, 147, 122-135,
doi:10.1016/j.quascirev.2016.02.011, 2016.
- Bécel, A., Shillington, D. J., Delescluse, M., Nedimović, M. R., Abers, G. A., Saffer, D. M., and Kuehn, H.: Tsunamigenic
655 structures in a creeping section of the Alaska subduction zone, *Nat. Geosci.*, 10(8), 609-613, doi: 10.1038/ngeo2990, 2017.
- Bellwald, B., Hjelstuen, B. O., Sejrup, H. P., and Haflidason, H.: Postglacial mass movements and depositional environments
in a high-latitude fjord system—Hardangerfjorden, Western Norway, *Mar. Geol.*, 379, 157-175, doi:
10.1016/j.margeo.2016.06.002, 2016.
- Berkhoff, J.C.W.: Computation of combined refraction-diffraction, in *Coastal Engineering*, 471-490, 1972.
- 660 Berndt, C., Brune, S., Nisbet, E., Zschau, J., and Sobolev, S. V.: Tsunami modelling of a submarine landslide in the Fram
Strait, *Geochem. Geophys.*, 10 (4), doi:10.1029/2008GC002292, 2009.

- Blikra, L. H., Longva, O., Harbitz, C., and Løvholt, F: Quantification of rock-avalanche and tsunami hazard in Storfjorden, western Norway. London, 2005.
- 665 Böhme, M., Oppikofer, T., Longva, O., Jaboyedoff, M., Hermanns, R. L., and Derron, M. H: Analyses of past and present rock slope instabilities in a fjord valley: Implications for hazard estimations. *Geomorphology*, 248, 464-474, doi: 10.1016/j.geomorph.2015.06.045, 2015.
- Bondevik, S., Mangerud, J., Dawson, S., Dawson, and A., Lohne, Ø.: Record-breaking height for 8000-year-old tsunami in the North Atlantic, *EOS*, 84 (31), 289-297, doi: 10.1029/2003EO310001, 2003.
- 670 Bondevik, S., Stormo, S. K., and Skjerdal, G.: Green mosses date the Storegga tsunami to the chilliest decades of the 8.2 ka cold event, *Quat. Sci. Rev.*, 45, 1-6, doi:10.1016/j.quascirev.2012.04.020, 2012.
- Brunet, M., Moretti, L., Le Friant, A., Mangeney, A., Fern´andez Nieto, E.D., and Bouchut, F.: Numerical simulation of the 30–45 ka debris avalanche flow of Montagne Pel´ee volcano, Martinique: from volcano flank collapse to submarine emplacement, *Nat. Hazards*, 87, 1189–1222, doi: 10.1007/s11069-017-2815-5, 2017.
- Bryn, P., Berg, K., Forsberg, C. F., Solheim, A., and Kvalstad, T. J.: Explaining the Storegga Slide *Mar. Pet. Geol.*, 22(1-2), 675 11-19, doi:10.1016/B978-0-08-044694-3.50005-6, 2005.
- Bugge, T., Befring, S., Belderson, R.H., Eidvin, T., Jansen, E., Kenyon, N., Holtedahl, H., and Sejrup, H.P.: A giant three-stage submarine slide off Norway, *Geo-Marine Letters*, 7, 191–198, 1987.
- Butt, F.A., Elverhøi, A., Solheim, A., and Forsberg, C.F.: Deciphering late Cenozoic development of the western Svalbard Margin from ODP Site 986 results, *Mar. Geol* 169 (3-4), 373–390, doi:10.1016/S0025-3227(00)00088-8, 2000.
- 680 Canals, M., Lastras, G., Urgeles, R., Casamor, J. L., Mienert, J., Cattaneo, A., De Batist, M., Haflidason, H., Imbo, Y., Laberg, J. S., Locat, J., Long, D., Longva, O., Masson, D. G., Sultan, N., Trincardi, F., and Bryn, P.: Slope failure dynamics and impacts from seafloor and shallow sub-seafloor geophysical data: case studies from the COSTA project, *Mar. Geol.*, 213(1-4), 9–72, doi: 10.1016/j.margeo.2004.10.001, 2004.
- Casas, D., Chiocci, F., Casalbore, D., Ercilla, G., & De Urbina, J. O. (2016). Magnitude-frequency distribution of submarine 685 landslides in the Gioia Basin (southern Tyrrhenian Sea). *Geo-Marine Letters*, 36(6), 405-414.
- Casas, D., Ercilla, G., Garc´ia, M., Yenes, M., and Estrada, F.: Post-rift sedimentary evolution of the Gebra Debris Valley. A submarine slope failure system in the Central Bransfield Basin (Antarctica), *Mar Geol*, 340, 16-29, doi: 10.1016/j.margeo.2013.04.011, 2013.
- Castro D´iaz, M. J., and Fern´andez-Nieto, E.: A class of computationally fast first order finite volume solvers: PVM methods, 690 *SIAM, J.Sci. Comput.*, 34(4), A2173-A2196, doi: 10.1137/100795280, 2012.
- Castro, M. J., Ortega, S., De la Asuncion, M., Mantas, J. M., and Gallardo, J. M.: GPU computing for shallow water flow simulation based on finite volume schemes, *C. R. Mec.*, 339(2-3), 165-184, doi: 10.1016/j.crme.2010.12.004, 2011.
- Chiocci, F. L., & Casalbore, D. (2017). Unexpected fast rate of morphological evolution of geologically-active continental margins during Quaternary: Examples from selected areas in the Italian seas. *Marine and Petroleum Geology*, 82, 154-162.

- 695 Chiocci, F. L., and Ridente, D.: Regional-scale seafloor mapping and geohazard assessment. The experience from the Italian project MaGIC (Marine Geohazards along the Italian Coasts), *Mar. Geophys. Res.*, 32(1), 13-23, doi: 10.1007/s11001-011-9120-6, 2011.
- Dietrich, A., and Krautblatter, M.: Deciphering controls for debris-flow erosion derived from a LiDAR-recorded extreme event and a calibrated numerical model, *Earth Surf. Process. Landf.*, 44(6), 1346-1361, doi: doi.org/10.1002/esp.4578, 2019.
- 700 Eck, M., and Hoppe, H.: Automatic reconstruction of B-spline surfaces of arbitrary topological type, In *Proceedings of the 23rd annual conference on Computer Graphics and Interactive Techniques*, 325-334, 1996.
- Eiken, O.: *Seismic Atlas of Western Svalbard*, Norsk Polarinstituttts Meddelelser, 130, 73, ISBN, 82-7666-067-3, 1994.
- Elverhøi, A., de Blasio, A., Butt, F.A., Issler, F.A., Harbitz, d., Engvik, L., Solheim, A., and Marr, J.: Submarine mass-wasting on glacially-influenced continental slopes: processes and dynamics, *J. Geol Soc London*, 203, 73-87, 705 doi:10.1144/GSL.SP.2002.203.01.05, 2002.
- Engen, Ø., Faleide, J. I., and Dyreng, T. K.: Opening of the Fram Strait gateway: A review of plate tectonic constraints, *Tectonophysics*, 450 (1), 51–69, doi: 10.1016/j.tecto.2008.01.002, 2008.
- Ercilla, G., Casas, D., Alonso, B., Casalbore, D., Estrada, F., Idárraga-García, J., López-González, N., Pedrosa, M., Teixeira, M., Sánchez-Guillamón, O., Azpiroz-Zabala, M., Bárcenas, P., Chiocci, F. L., García, M., Galindo-Zaldívar, J., Geyer, A., 710 Gómez-Ballesteros, M., Juan, C., Martorelli, and E., Yenes, M.: *Deep Sea Sedimentation (J. (Jack) F. B. T.T. on G. (Second E. Shroder (ed.); (960–988), 2022, Academic Press, doi 10.1016/B978-0-12-818234-5.00129-2, 2022.*
- Escalante, C., Morales de Luna, T., and Castro, M. J.: Non-hydrostatic pressure shallow flows: GPU implementation using finite volume and finite difference scheme, *Applied Mathematics and Computation*, 338, 631-659, doi: 10.1016/j.amc.2018.06.035, 2018.
- 715 Escalante, C., Dumbser, M., and Castro, M. J.: An efficient hyperbolic relaxation system for dispersive non-hydrostatic water waves and its solution with high order discontinuous Galerkin schemes, *Journal of Computational Physics*, 394, 385-416, doi: 10.1016/j.jcp.2019.05.035, 2019.
- Estrada, F., González-Vida, J. M., Peláez, J. A., Galindo-Zaldívar, J., Ortega, S., Macías, J., and Ercilla, G.: Tsunami generation potential of a strike-slip fault tip in the westernmost Mediterranean, *Sci. Rep.* 11(1), 1-9, doi: 10.1038/s41598-720 021-95729-6, 2021.
- Faleide, J. I., Vågnes, E., and Gudlaugsson, S. T.: Late Mesozoic–Cenozoic evolution of the southwestern Barents Sea in a regional rift-shear tectonic setting, *Mat. Pet. Geol.*, 10(3), 186-214, doi: 10.1016/0264-8172(93)90104-Z, 1993.
- Faleide, J.I., Tsikalas, F., Breivik, A.J., Mjelde, R., Ritzmann, O., Wilson, J., and Eldholm, O.: Structure and evolution of the continental margin off Norway and the Barents Sea, 31, 82–91, doi: 10.18814/epiugs/2008/v31i1/012, 2008.
- 725 Fernández-Nieto, E., Parisot, M., Penel, Y., and Sainte-Marie, J.: A hierarchy of dispersive layer-averaged approximations of Euler equations for free surface flows, *Communications in Mathematical Sciences* 16, 1169–1202, 2018.
- Fernández-Nieto, E.D., Bouchut, F., Bresch, D. Castro., and M.J., Mangeney, A.: A new Savage–Hutter type model for submarine avalanches and generated tsunamis, *J. Comput. Phys*, 227, 7720-775, doi: 10.1016/j.jcp.2008.04.039, 2008.

- Fiedler, A. and Faleide, J.I.: Cenozoic sedimentation along the southwestern Barents Sea margin in relation to uplift and erosion of the shelf, *Glob. Planet. Change*, 12, 75–93, doi: 10.1016/0921-8181(95)00013-5, 1996.
- 730 Fine, I. V., Rabinovich, A. B., Bornhold, B. D., Thomson, R. E., and Kulikov, E. A.: The Grand Banks landslide-generated tsunami of November 18, 1929: preliminary analysis and numerical modelling, *Mar. Geol.*, 215(1-2), 45-57, doi: 10.1016/j.margeo.2004.11.007, 2005.
- Førland, E. J., Jacobsen, J. K. S., Denstadli, J. M., Lohmann, M., Hanssen-Bauer, I., Hygen, H. O., and Tømmervik, H.: Cool weather tourism under global warming: Comparing Arctic summer tourists' weather preferences with regional climate statistics and projections, *Tourism Management*, 36, 567-579, doi:10.1016/j.tourman.2012.09.002, 2013.
- 735 Frey-Martínez, J., Cartwright, J., and James, D.: Frontally confined versus frontally emergent submarine landslides: A 3D seismic characterization, *Mar. Pet. Geol.*, 23(5), 585-604, doi:10.1016/j.marpetgeo.2006.04.002, 2006.
- Fryer, G. J., Watts, P., and Pratson, L. F.: Source of the great tsunami of 1 April 1946: a landslide in the upper Aleutian forearc, *Mar. Geol.*, 203(3-4), 201-218, doi: 10.1016/S0025-3227(03)00305-0, 2004.
- 740 García, M., Ercilla, G., and Alonso, B.: Morphology and sedimentary systems in the Central Bransfield Basin, Antarctic Peninsula: sedimentary dynamics from shelf to basin, *Basin. Res.*, 21(3), 295-314, doi: 10.1111/j.1365-2117.2008.00386.x, 2009.
- García, M., Ercilla, G., Alonso, B., Casas, D., and Dowdeswell, J. A.: Sediment lithofacies, processes and sedimentary models in the Central Bransfield Basin, Antarctic Peninsula, since the Last Glacial Maximum, *Mar. Geol.*, 290(1), 1–16, doi: 10.1016/j.margeo.2011.10.006, 2011.
- 745 González-Vida, J. M., Macías, J., Castro, M. J., Sánchez-Linares, C., de la Asunción, M., Ortega-Acosta, S., and Arcas, D.: The Lituya Bay landslide-generated mega-tsunami—numerical simulation and sensitivity analysis, *Natural Hazards and Earth System Sciences*, 19(2), 369-388, doi: 10.5194/nhess-19-369-2019, 2019.
- 750 Haflidason, H., Sejrup, H. P., Nygård, A., Mienert, J., Bryn, P., Lien, R., and Masson, D.: The Storegga Slide: architecture, geometry and slide development, *Marine geology*, 213(1-4), 201-234, doi: 10.1016/j.margeo.2004.10.007, 2004.
- Haflidason, H., Lien, R., Sejrup, H. P., Forsberg, C. F., and Bryn, P.: The dating and morphometry of the Storegga Slide, *Mar.Pet. Geol.*, 22 (1), 123–136, doi:10.1016/j.marpetgeo.2004.10.008, 2005.
- Hampel, A., Hetzel, R., Maniatis, G., and Karow, T.: Three-dimensional numerical modelling of slip rate variations on normal and thrust fault arrays during ice cap growth and melting, *J. Geophys. Res.*, 114 (B8) 406, doi: 10.1029/2008JB006113, 2009.
- 755 Harbitz, C. B., Løvholt, F., Pedersen, G., and Masson, D. G.: Mechanisms of tsunami generation by submarine landslides: a short review, *N. J. Geol*, 86(3), 2006.
- Huggel, C., Zraggen-Oswald, S., Haeberli, W., Käab, A., Polkvoj, A., Galushkin, I., and Evans, S. G.: The 2002 rock/ice avalanche at Kolka/Karmadon, Russian Caucasus: assessment of extraordinary avalanche formation and mobility, and application of QuickBird satellite imagery, *Nat. Hazards Earth Syst. Sci*, 5(2), 173-187, doi: 10.5194/nhess-5-173-2005, 2005.
- 760

- Iglesias, O., Lastras, G., Canals, M., Olabarrieta, M., Gonzalez, M., Aniel-Quiroga, Í., and De Mol, B.: The BIG'95 submarine landslide-generated tsunami: a numerical simulation, *The Journal of Geology*, 120(1), 31-48, doi: 10.1086/662718, 2012.
- 765 Imamura, F., Boret, S. P., Suppasri, A., and Muhari, A.: Recent occurrences of serious tsunami damage and the future challenges of tsunami disaster risk reduction, *Progress in Disaster Science*, 1, 100009, doi: 10.1016/j.pdisas.2019.100009, 2019.
- Innocenti, C., Battaglini, L., D'Angelo, S., and Fiorentino, A.: Submarine landslides: mapping the susceptibility in European seas, *Q. J. Eng. Geol. Hydrogeol.*, 54(1), doi:10.1144/qjegh2020-027, 2021.
- 770 Ioualalen, M., Rentería, W., Ilayaraja, K., Chlieh, M., Arreaga-Vargas, P.: A synoptic picture of the impact of the 26th December 2004 Indian Ocean tsunami on the coast of Sri Lanka, *Environmental modelling software*, 25(12), 1874-1880, doi: 10.1016/j.envsoft.2010.04.010, 2010.
- Knies, J., Matthiessen, J., Vogt, C., Laberg, J.S., Hjelstuen, B.O., Smelror, M., Larsen, E., Andreassen, K., Eidvin, T., Vorren, T.O.: The Plio-Pleistocene glaciation of the Barents Sea–Svalbard region: a new model based on revised chronostratigraphy, *Quat. Sci. Rev.*, 28, 812–829, doi:10.1016/j.quascirev.2008.12.002, 2009.
- 775 Kvalstad, T. J., Andresen, L., Forsberg, C. F., Berg, K., Bryn, P., and Wangen, M.: The Storegga slide: evaluation of triggering sources and slide mechanics, Editor(s): Solheim, A., Bryn, P., Berg, K., Sejrup, H. PMIENERT., J, Ormen Lange—an Integrated Study for Safe Field Development in the Storegga Submarine Area, Elsevier, 245–256, doi: 10.1016/B978-0-08-044694-3.50025-1, 2005.
- 780 L'Heureux, J.S., Vanneste, M., Rise, L., Brendryen, J., Forsberg, C.F., Nadim, F., Longva, O., Chand, S., Kvalstad, T.J., and Haflidason, H.: Stability, mobility and failure mechanism for landslides at the upper continental slope off Vesterålen, Norway, *Mar. Geol.* 346, 192–207, doi:10.1016/j.margeo.2013.09.009, 2013.
- Laberg, J.S., Vorren, T.O., Dowdeswell, J.A., Kenyon, N.H., and Taylor, J.: The Andøya Slide and the Andøya Canyon, north-eastern Norwegian–Greenland Sea, *Mar Geol*, 162(2-4), 259-275, 2000.
- 785 Laberg, J.S., and Vorren, T.O.: A Late Pleistocene submarine slide on the Bear Island Trough Mouth Fan, *Geo-Mar. Lett.*, 13, 227–234, doi:10.1007/BF01207752, 1993.
- Lee, H. J.: Timing of occurrence of large submarine landslides on the Atlantic Ocean margin, *Mar. Geol.*, 264(1–2), 53–64, doi: 10.1016/j.margeo.2008.09.009, 2009.
- Lee, S., Wolberg, G., and Shin, S. Y.: Scattered data interpolation with multilevel B-splines, *IEEE transactions on visualization and computer graphics*, 3(3), 228-244, doi: 10.1109/2945.620490, 1997.
- 790 León, R., Llorente, M., and Giménez-Moreno, C. J.: Marine Gas Hydrate Geohazard Assessment on the European Continental Margins. The Impact of Critical Knowledge Gaps, *Appl. Sci.*, 11(6), 2865, doi: 10.3390/app11062865, 2021.
- Lindberg, B., Laberg, J. S., and Vorren, T. O.: The Nyk Slide—morphology, progression, and age of a partly buried submarine slide offshore northern Norway, *Mar. Geol.*, 213(1-4), 277-289, doi: 10.1016/j.margeo.2004.10.010, 2004.

- 795 Llopart, J. Storfjorden Trough Mouth Fan (Western Barents Sea): Slope Failures in Polar Continental Margins; Significance of Stress Changes and Fluid Migration Induced by Glacial Cycles, PhD thesis, Universitat de Barcelona, pp. 231, <http://hdl.handle.net/2445/108581>, 2016.
- Llopart, J., Urgeles, R., Camerlenghi, A., Lucchi, R.G., Rebesco, M., and De Mol, B.: Late Quaternary development of the Storfjorden and Kveithola Trough Mouth Fans, northwestern Barents Sea, *Quat. Sci. Rev.* 129, 68–84, 2012, doi: 10.1016/j.quascirev.2015.10.002, 2015.
- 800 Llopart, J., Urgeles, R., Forsberg, C. F., Camerlenghi, A., Vanneste, M., Rebesco, M., and Lantzsch, H.: Fluid flow and pore pressure development throughout the evolution of a trough mouth fan, western Barents Sea, *Basin Research*, 31(3), 487-513, doi:10.1111/bre.12331, 2019.
- Løvholt, F., Glimsdal, S., and Harbitz, C. B.: On the landslide tsunami uncertainty and hazard, *Landslides*, 17(10), 2301-2315, doi: 10.1007/s10346-020-01429-z, 2020.
- 805 Løvholt, F., Pedersen, G., Harbitz, C. B., Glimsdal, S., and Kim, J.: On the characteristics of landslide tsunamis, *Phil. Trans. R. Soc. A*.3732014037620140376, doi:10.1098/rsta.2014.0376, 2015.
- Lucchi, R. G., Camerlenghi, A., Rebesco, M., Colmenero-Hidalgo, E., Sierro, F. J., Sagnotti, L., and Caburlotto, A.: Postglacial sedimentary processes on the Storfjorden and Kveithola trough mouth fans: Significance of extreme glacial marine sedimentation, *Glob. Planet. Change*, 111, 309-326, doi:10.1016/j.gloplacha.2013.10.008, 2013.
- 810 Lucchi, R.G., Pedrosa, M.T., Camerlenghi, A., Urgeles, R., De Mol, B., and Rebesco, M.: Recent submarine landslides on the continental slope of Storfjorden and Kveithola Trough-Mouth Fans (North West Barents Sea). In: Yamada, Y., Kawamura, K., Ikehara, K., Ogawa, Y., Urgeles, R., Mosher, D., Chaytor, J., Strasser, M. (Eds.), *Submarine Mass Movement and Their Consequences*, *Advances in Natural and Technological Hazards Research*. 31. Springer, Dordrecht (The Netherlands), pp. 735–745, 2012, doi: 10.1007/978-94-007-2162-3_65, 2012.
- 815 Macías, J., Vázquez, J. T., Fernández-Salas, L. M., González-Vida, J. M., Bárcenas, P., Castro, M. J., Díaz-del-Río, V., and Alonso, B.: The Al-Borani submarine landslide and associated tsunamis, A modelling approach, *Mar. Geol.* 361, 79–95, doi: 10.1016/j.margeo.2014.12.006, 2015.
- Maslin, M., Mikkelsen, N., Vilela, C., and Haq, B.: Sea-level–and gas-hydrate–controlled catastrophic sediment failures of the Amazon Fan, *Geology*, 26(12), 1107-1110, doi: 10.1130/0091-7613(1998)026<1107:SLAGHC>2.3.CO;2, 1998.
- 820 Meleshko, V. P., Golitsyn, G. S., Govorkova, V. A., Demchenko, P. F., Eliseev, A. V., Kattsov, V. M., and Sporyshev, P. V.: Anthropogenic climate change in Russia in the 21st century: An ensemble of climate model projections, *Meteorologiya i gidrologiya*, 4, 38-49, 2004.
- Moernaut, J., and De Batist, M.: Frontal emplacement and mobility of sublacustrine landslides: results from morphometric and seismostratigraphic analysis, *Mar. Geol.* 285(1-4), 29-45, doi: 10.1016/j.margeo.2011.05.001, 2011.
- 825 Moernaut, J., Van Daele, M., Strasser, M., Clare, M. A., Heirman, K., Viel, M., Cardenas, J., Kilian, R., Ladrón de Guevara, B., Pino, M., Urrutia, R., and De Batist, M.: Lacustrine turbidites produced by surficial slope sediment remobilization: A

- mechanism for continuous and sensitive turbidite paleoseismic records, *Mar. Geol.*, 384, 159-176. doi:10.1016/j.margeo.2015.10.009, 2017.
- 830 Newton, A. M., and Huuse, M.: Glacial geomorphology of the central Barents Sea: implications for the dynamic deglaciation of the Barents Sea Ice Sheet, *Mar. Geol.*, 387, 114-131, doi:10.1016/j.margeo.2017.04.001, 2017.
- Ottesen, D., Dowdeswell, J.A., and Rise, S.: Submarine landforms and the reconstruction of fast-flowing ice streams within a large Quaternary ice sheet: The 2500-km-long Norwegian-Svalbard margin (57°–80°N), *Geol. Soc. Am. Bull.*, 117, 1033–1050, doi: doi.org/10.1130/B25577.1, 2005.
- 835 Pedrosa, M. T., Camerlenghi, A., De Mol, B., Urgeles, R., Rebesco, M., and Lucchi, R. G.: Seabed morphology and shallow sedimentary structure of the Storfjorden and Kveithola trough-mouth fans (North West Barents Sea), *Mar. Geol.*, 286(1-4), 65-81, doi: 10.1016/j.margeo.2011.05.009, 2011.
- Piper, D. J., Cochonat, P., and Morrison, M. L.: The sequence of events around the epicentre of the 1929 Grand Banks earthquake: initiation of debris flows and turbidity current inferred from sidescan sonar, *Sedimentology*, 46(1), 79-97, doi: 10.1046/j.1365-3091.1999.00204.x, 1999.
- 840 Pirli, M., Schweitzer, J., and Paulsen, B.: The Storfjorden, Svalbard, 2008–2012 aftershock sequence: Seismotectonics in a polar environment, *Tectonophysics*, 601, 192–205. doi:10.1016/j.tecto.2013.05.010, 2013.
- Pouliquen, O., and Forterre, Y.: Friction law for dense granular flows: application to the motion of a mass down a rough inclined plane, *Journal of fluid mechanics*, 453, 133-151, doi: 10.1017/S0022112001006796, 2002.
- 845 Pudasaini, S. P.: Dynamics of submarine debris flow and tsunami, *Acta Mechanica*, 225(8), 2423-2434, doi: 10.1007/s00707-014-1126-0, 2014.
- Ramadan, K.T.: Near- and far-field tsunami waves, displaced water volume, potential energy and velocity flow rates by a stochastic submarine earthquake source model, *Nat. Hazards Earth Syst. Sci. Discuss*, doi: 10.5194/nhess-2018-107, 2018.
- Rebesco, M., Laberg, J. S., Pedrosa, M. T., Camerlenghi, A., Lucchi, R. G., Zgur, F., and Wardell, N.: Onset and growth of 850 Trough-Mouth Fans on the North-Western Barents Sea margin -implications for the evolution of the Barents Sea/Svalbard Ice Sheet, *Quat. Sci. Rev.*, 92, 227–234, doi:10.1016/j.quascirev.2013.08.015, 2013.
- Rebesco, M., Pedrosa, M.T., Camerlenghi, A., Lucchi, R.G., Sauli, C., De Mol, B., Madrussani, G., Urgeles, R., Rossi, G., and Böhm, G.: One million years of climatic generated landslide events on the northwestern Barents Sea continental margin. In: Yamada, Y., Kawamura, K., Ikehara, K., Ogawa, Y., Urgeles, R., Mosher, D., Chaytor, J., Strasser, M. (Eds.), 855 *Submarine Mass Movements and Their Consequences. Advances in Natural and Technological Hazards Research*. 31, Springer, Dordrecht (The Netherlands), pp. 747–756, doi:10.1007/978-94-007-2162-3-66, 2012.
- Rodríguez-Morata, C., Villacorta, S., Stoffel, M., and Ballesteros-Cánovas, J. A.: Assessing strategies to mitigate debris-flow risk in Abancay province, south-central Peruvian Andes, *Geomorphology*, 342, 127–139, doi:10.1016/j.geomorph.2019.06.012, 2019.
- 860 Salaree, A and Okal, E.: Effects of bathymetry complexity on tsunami propagation: a spherical harmonics approach, *Geophysical Journal International*, 223, 632-647, doi:10.1093/gji/ggaa334, 2020.

- Shonting, D., and Ezrailson, C.: The Chicxulub Tsunami, In: *Chicxulub: The Impact and Tsunami*, Springer, Praxis, Book, Cham, 69-106, doi: 10.1007/978-3-319-39487-9_4, 2017.
- 865 Sierro, F. J., Andersen, N., Bassetti, M. A., Berné, S., Canals, M., Curtis, J. H., Dennielou, B., Flores, J. A., Frigola, J., Gonzalez-Mora, B., Grimalt, J. O., Hodell, D. A., Jouet, G., Pérez-Folgado, M., and Schneider, R.: Phase relationship between sea level and abrupt climate change, *Quat. Sci. Rev.*, 28(25), 2867–2881, doi: 10.1016/j.quascirev.2009.07.019, 2009.
- 870 Skogseth, R., Olivier, L. L., Nilsen, F., Falck, E., Fraser, N., Tverberg, V., and Falk-Petersen, S.: Variability and decadal trends in the Isfjorden (Svalbard) ocean climate and circulation—An indicator for climate change in the European Arctic, *Prog. Oceanogr.*, 187, 102394, doi:10.1016/j.pocean.2020.102394, 2020.
- Solheim, A., Berg, K., Forsberg, C. F., and Bryn, P.: The Storegga Slide complex: repetitive large scale sliding with similar cause and development, *Marine and Petroleum Geology*, 22(1-2), 97-107, doi.org:10.1016/j.marpetgeo.2004.10.013, 2004.
- Sun, Q., and Leslie, S.: Tsunamigenic potential of an incipient submarine slope failure in the northern South China Sea, *Mar. Pet. Geol.*, 112, 104111. doi: 10.1016/j.marpetgeo.2019.104111, 2020.
- 875 Synolakis, C. E., Yalciner, A. C., Borrero, J. C., and Plafker, G.: Modelling of the November 3, 1994 Skagway, Alaska tsunami, In *Solutions to Coastal Disasters*, 915-927, 2002.
- Talling, P. J.: On the triggers, resulting flow types and frequencies of subaqueous sediment density flows in different settings: *Mar. Geol.*, 352, 155-182, doi:10.1016/j.margeo.2014.02.006, 2014.
- 880 Tappin, D. R.: Submarine mass failures as tsunami sources: their climate control, *Phil. Trans. R. Soc. A*, 368(1919), 2417-2434, doi:10.1098/rsta.2010.0079, 2010.
- Thomson, R. E., Rabinovich, A. B., Kulikov, E. A., Fine, I. V., and Bornhold, B. D.: On numerical simulation of the landslide-generated tsunami of November 3, 1994 in Skagway Harbor, Alaska. In *Tsunami research at the end of a critical decade*, 243-282, Springer, Dordrecht, doi: 10.1007/978-94-017-3618-3_17, 2001.
- 885 Tinti, S., Bortolucci, E., and Romagnoli, C.: Computer simulations of tsunamis due to sector collapse at Stromboli, Italy, *Journal of Volcanology and Geothermal Research*, 96(1-2), 103-128, doi: 10.1016/S0377-0273(99)00138-9, 2000.
- Urgeles, R., Bahk, J. J., Lee, S. H., Horozal, S., Cukur, D., Kim, S. P., Kim, J.Y., S.W, Jeong., I.K., U.: Tsunami hazard from submarine landslides: scenario-based assessment in the Ulleung Basin, East Sea (Japan Sea), *Geoscience Journal*, 23, 439–460, doi: 10.1007/s12303-018-0044-x, 2019.
- 890 Urlaub, M., Talling, P.J., and Masson, D.G.: Timing and frequency of large submarine landslides: implications for understanding triggers and future geohazard, *Quat. Sci. Rev.*, 72, 63–82, doi:10.1016/j.quascirev.2013.04.020, 2013.
- Vanneste, M., Mienert, J., and Bünz, S.: The Hinlopen Slide: a giant, submarine slope failure on the northern Svalbard margin, *Arctic Ocean, EARTH & PLANET. SCI. LETT.*, 245(1-2), 373-388, doi: 10.1016/j.epsl.2006.02.045, 2006,
- 895 Vanneste, M., Harbitz, C. B., De Blasio, F. V., Glimsdal, S., Mienert, J., and Elverhøi, A.: Hinlopen-Yermak Landslide, Arctic Ocean Geomorphology, landslide dynamics and tsunami simulations, *Mass-Transport Deposits (in) Deepwater Settings*, edited by: Shipp, R., Weimer, P., and Posamentier, H, 96, 2011.

- Vanneste, M., Sultan, N., Garziglia, S., Forsberg, C. F., and L'Heureux, J. S.: Seafloor instabilities and sediment deformation processes: The need for integrated, multi-disciplinary investigations, *Mar. Geol.*, 352, 183-214, doi: 10.1016/j.margeo.2014.01.005, 2014.
- 900 Vázquez, J. T., Ercilla, G., Alonso, B., Peláez, J. A., Palomino, D., León, R., ... and La fuerza, S.: Triggering Mechanisms of Tsunamis in the Gulf of Cadiz and the Alboran Sea: An Overview, in: *Historical Earthquakes, Tsunamis and Archaeology in the Iberian Peninsula (Natural Science in Archaeology)*, edited by: Álvarez-Martí-Aguilar, M., and Prieto, F. M., Springer, Singapore, 65-104, https://doi.org/10.1007/978-981-19-1979-4_4, 2022.
- Waddington, C., and Wicks, K.: Resilience or wipe out? Evaluating the convergent impacts of the 8.2 ka event and Storegga tsunami on the Mesolithic of northeast Britain, *J. Archaeol. Sci. Rep.*, 14, 692-714, doi: 10.1016/j.jasrep.2017.04.015, 2017.
- 905 Watt, S. F. L., Talling, P. J., Vardy, M. E., Masson, D. G., Henstock, T. J., Hühnerbach, V., and Karstens, J.: Widespread and progressive seafloor-sediment failure following volcanic debris avalanche emplacement: Landslide dynamics and timing offshore Montserrat, Lesser Antilles, *Marine Geology*, 323, 69-94, doi: 10.1016/j.margeo.2012.08.002, 2012.
- Winkelmann, D., Geissler, W., Schneider, J., and Stein, R.: Dynamics and timing of the Hinlopen/Yermak Megaslide north of Spitsbergen, Arctic Ocean, *Mar. Geol.*, 250(1), 34–50, doi: 10.1016/j.margeo.2007.11.013, 2012.
- 910 Worsley, D., Aga, O.J., Dalland, A., Elverhøi, A., and Thon, A.: The Geological History of Svalbard, Evolution of an Arctic Archipelago, Statoil, Asker Trykkeri, Stavanger, 121, 1986.
- Zhang, W., Almgren, A., Beckner, V., Bell, J., Blaschke, J., Chan, C., and Zingale, M.: AMReX: a framework for block-structured adaptive mesh refinement, *J. Open. Source. Softw.*, 4(37), 1370-1370, doi: 10.21105/joss.01370, 2019.